VAHUR ZADIN

Modelling
the 3D-microbattery

Institue of Technology, University of Tartu, Estonia

Dissertation is accepted for the commencement of the degree of Doctor of Philosophy (Physical Engineering) on April 24th, 2012 the council of Institute of Technology, Faculty of Science and Technology, University of Tartu.

Supervisors:	Prof. Alvo Aabloo, PhD Insitute of Technology Faculty of Science and Technology University of Tartu, Estonia
	Heiki Kasemägi, PhD Insitute of Technology Faculty of Science and Technology University of Tartu, Estonia
External supervisor:	Daniel Brandell, PhD Department of Chemistry, Ångström Uppsala University, Sweden
Opponent:	Mårten Behm, PhD KTH Royal Institute of Technology Sweden

Commencement: Auditorium 121, Nooruse 1, Tartu, Estonia, at 14:15 on June 8th, 2012

Publication of this dissertation is granted by University of Tartu

European Union
European Social Fund

Investing in your future

CONTENTS

LIST OF PUBLICATIONS

This thesis summarizes following papers:

I. V. Zadin, D. Danilov, D. Brandell, P.H.L. Notten, A. Aabloo, Finite element simulations of 3D ionic transportation properties in Li-ion electrolytes, *Electrochimica Acta*, **65** (2012) 165–173.

II. V. Zadin, D. Brandell, H. Kasemägi, A. Aabloo, J.O. Thomas, Finite element modelling of ion transport in the electrolyte of a 3D-microbattery, *Solid State Ionics*, **192** (2011) 279–283.

III. V. Zadin, H. Kasemägi, A. Aabloo, D. Brandell, Modelling electrode material utilization in the trench model 3D-microbattery by finite element analysis, *Journal of Power Sources*, **195** (2010) 6218–6224.

IV. V. Zadin, D. Brandell, Modelling polymer electrolytes for 3D-microbatteries using finite element analysis, *Electrochimica Acta*, **57** (2011) 237–243.

V. V. Zadin, D. Brandell, H. Kasemägi, J. Lellep, A. Aabloo, Designing the 3D-microbattery geometry using the level-set method, *submitted to Physical Chemistry Chemical Physics*.

Authors contribution

The author of this thesis is responsible for majority of the research in all phases (including writing, simulations and preparation of images) of Papers **I–V**. The planning of the work and derivation of the theoretical results in Paper **I** is shared effort with Dr. D. Danilov.

ABBREVIATIONS AND SYMBOLS

MEMS	Microelectromechanical systems
3D-MB	3D-microbattery
LHS	Left Hand Side
RHS	Right Hand Side
FEM	Finite Element Method
PDE	Partial Differential Equation
SIMP	Solid Isotropic Material with Penalization
MD	Molecular Dynamics
SEI	Solid Electrolyte Interface
a	Specific area of an electrode (m^{-1})
c	Concentration (mol/m^3)
D	Diffusion coefficient (m^2/s)
F	Faraday constant (96 487 C/mol)
H,h,d,d_c	Geometrical parameters of the cell (Table 1)
i_0	Exchange current density (A/m^2)
J	Ionic flux density (mol/(m^2s))
k	Rate constant (m/s)
r	Normalized resistance of the cell (Ω m^2)
R	Universal gas constant (8.314 J/(mol K))
T	Absolute Temperature (K)
V	Volume of the electrolyte (m^3)
V_{oc}	Open circuit voltage (V)
z	Charge number
$\vec{j}$	Current density (A/m^2)
t_+^0	Transference number of Li^+ ions in the electrolyte
$\vec{n}$	Unit normal vector

Greek letters

ϕ	The level-set function
α	Transfer coefficient
γ	Reinitalization parameter (m/s)
$\delta(x)$	Dirac delta function
ε	Porosity of the electrodes
ε_{ls}	Electrode-electrolyte interface thickness during optimization (m)
η	Surface overpotential in the battery (V)
λ	Lagrange multiplier (A/m^2)
σ	Conductivity (S/m)
φ	Electrical potential (V)
Ω	Geometrical region of the problem (m)
τ	Pseudo time, representing the optimization step

Subscripts

Li	Li^+ ions
PF$_6$	PF_6^- ions
0	Corresponding to constant initial value or boundary condition
a	Anodic
c	Cathodic
i	Defined when used
j	Defined when used
l	Liquid phase (electrolyte)
s	Solid phase (electrode material)
Opt	Optimized cell
Nonopt	Nonoptimized (reference) cell

Superscripts

p	Positive electrode
n	Negative electrode
*	Electrodes

1. INTRODUCTION

1.1. Towards small scale power sources

The history of electrochemical energy storage dates back to the years around 1800, when Italian scientist Alessandro Volta invented the first primary (*i.e.,* non-rechargeable) battery [1]. The first secondary (rechargeable) battery, the lead acid battery was invented more than half a century later, in 1859 by the French physicist Gaston Planté [2,3]. The first primary lithium batteries were commercialized in 1970s and the first modern Li-ion battery material, $LiCoO_2$, was introduced by Goodenough *et al.* in 1980 [4]. In 1991, the first commercial Li-ion battery was released by Sony, utilizing graphite as negative electrode. Today, the Li batteries comprise the battery technology with the highest energy density among the rechargeable chemistries.

A rapid technological development towards miniaturization of the electronic devices can be seen today. For example, computer processors already contain millions of transistors - a desktop computer with Intel Core i7–920 processor has 731 million transistors in 263 mm^2 [5]. Small scale devices, in dimensions of 1 mm^3 utilizing such electronics need power sources in their own dimensions. Unfortunately, the development of small scale power sources is far outpaced by the development of microelectronics. Currently, there are no micro-batteries constructed which combine high capacity and high battery current on a small footprint area. As a result, the current microbattery technology is a weak link in the development of the small scale autonomous technologies. One way to overcome this problem is to use the concept of a three dimensional microbattery (3D-MB), which would combine otherwise contradictory concepts of high current and high capacity properties [6]. Success in the development of the 3D-MBs would most likely enable a fast development in the fields of small scale medical devices, microrobotics, microelectomechanical devices (MEMS), *etc*.

However, the electrochemical properties of a battery with three-dimensional electrodes are radically different than for a two-dimensional architecture. The electrochemical activity, which is uniformly distributed over the surfaces in conventional cells with planar electrodes, obtains a nonuniform distribution in a three dimensional design, thereby causing nonuniform current densities [7]. This behavior can seriously reduce the performance of the 3D-cells and in worst case eliminate the advantages of the 3D architecture completely.

1.2. Limitations of the conventional battery architectures

The lithium-ion battery is an electrochemical device which consists of anode (generally lithium intercalated graphite), electrolyte (polymer or liquid) and

cathode (LiCoO$_2$, LiFePO$_4$, *etc.*). During discharge, electrons travel from anode to cathode through an external circuit while Li$^+$ ions move through the electrolyte. During charge, the processes are reversed. Currently, the Li-ion battery technology provides rechargeable cells with the highest energy density and voltage, but unfortunately, the existing thin-film microbatteries can only deliver either high energy storage (high capacity) or high power (high current), but fail to provide both at the same time [6,8].

Two types of battery electrodes are currently used – thin or thick film. Thin films provide high power, while thick films provide high capacity. Typical commercial lithium-ion batteries, used in devices like laptops or mobile phones, are thick film cells with porous composite electrodes. The active material in the electrodes is composed of small particles which are fixed in the electrodes with the help of binders. The electrodes are soaked with an electrolyte and separated by an electronically insulating separator. Typical thin film cells are usually designed for small scale applications and constructed using chemical or physical vapor technologies, where current collectors, electrodes and electrolyte are deposited layer-by-layer. The thickness of such cell is limited to a few micrometers.

A typical example of a simple MEMS device is an autonomous battery powered system, consisting of sensors, computation equipment and a communication circuit. The device needs a battery with total dimensions of 1–10 mm^3 – thereby requiring a "battery on a chip" [8]. A number of examples of such devices are presented in literature [9–12], and in all of these, the battery is at least several times larger than the rest of the device. The problems with the conventional two-dimensional (2D) battery design are directly revealed in these configurations: on a small foot-print area, it is not possible to achieve both sufficient energy storage and power for the device. The footprint area of the cell becomes the key of the miniaturization – thicker electrodes cannot be used to increase capacity since the mechanical integrity of such electrodes decreases and thicker films also reduces the power density by increasing resistivity. Winding the electrodes up would on the other hand lead to material fractures and short circuits [8]. In this context, the *capacity per footprint area* (Ahm^{-2}) becomes more important for microbatteries than the volumetric or gravimetric capacities which are common for conventional batteries. The compromise made by balancing the energy and power density in the thin film lithium-ion microbattery leads to limited capacities, generally in the range of 0.5 mAhcm^{-2} [13]. However, if the current 2D thin film battery technologies are improved, and the electrode structure is fabricated in 3D, the amount of electrode material per footprint area can be increased. The capacity of such a 3D cell should approach 10 mAhcm^{-2} [14].

1.3. The 3D-Microbattery

To illustrate the difference between a common thin film microbattery and a 3D-MB, consider a conventional thin film 2D-battery which can be represented by a sandwich structure, consisting of current collector, positive electrode, electrolyte (separator), negative electrode and current collector in a layer-by-layer configuration (Figure 1; not showing the current collectors). Since the electrodes are planar and the electrode-electrolyte surface area at each electrode is equal to the footprint area of the cell, the current density will be equal everywhere in the cell.
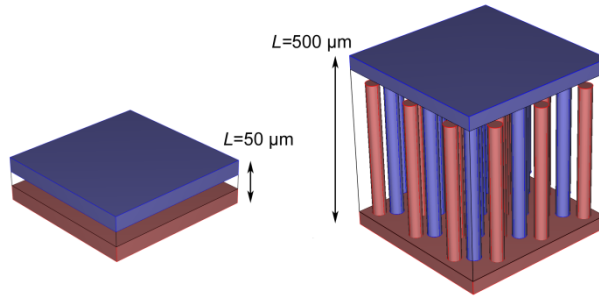

Figure 1. The difference between a conventional battery and a 3D-MB.

A 3D-MB, on the other hand, which consists of the same components but has a more complex spatial distribution and thereby an increased internal surface area, develops an inhomogeneous current density distribution [7]. Naturally, the increased internal surface area will decrease the local current density at the electrode-electrolyte interface (and generally in the cell), making it possible to use high current while at the same time providing high capacity. For example, a 3D-electrode with an order of magnitude larger electrode-electrolyte surface area than its footprint area would be able to provide up to 10 times larger current than a 2D battery with the same footprint area (the area the battery will occupy). The increased surface area will theoretically increase the power proportionally to the *area gain* achieved by incorporating 3D-electrodes. Area gain can be defined as the surface area of the 3D-electrode, divided with the footprint area of the 3D-cell.

The simple definition of a 3D-MB is: *a battery with three dimensional electrode structures*. However, this definition is not strict, since it does not capture all important features of the 3D-MB – the 3D-battery design should also incorporate short current transport pathways. For example, by using one 3D-electrode together with a planar lithium foil, a cell with a 3D electrode would be achieved, but its behavior would somewhat resemble a conventional porous thick film electrode. From a theoretical point of view, a *3D-MB is defined as a battery which has three dimensional and conformal electrode and electrolyte*

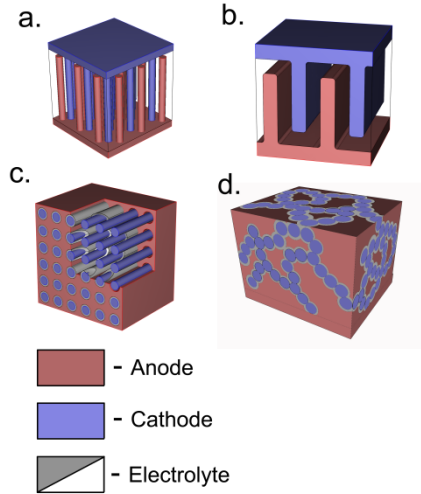*structure, making it possible to utilize all spatial directions in the charge and mass transport processes.*

Figure 2. Different 3D-MB architectures.

Examples of 3D-MB architectures currently under development are presented in Figure 2: 3D-interdigitated (a), 3D-trench (b), 3D-concentric (c) and aperiodic (d) architectures. However, a single optimal 3D-architecture has not yet evolved; all these different geometries are currently being developed and investigated by different 3D-MB researcher groups. The first experimental 3D batteries were presented by Golodnitsky *et al.* [15–17], where battery components were deposited on a perforated silicone substrate. The trench geometry (Figure 2b) is developed by for example Notten *et al.* [18–20], which have also investigated the interdigitated geometry (Figure 2a) [21]. In these studies, a silicone substrate with etched trenches was coated with a barrier layer to prevent Li diffusion into it, thereafter coated with a positive electrode layer. Micromachining was used to cut holes or trenches in the silicone or glass substrate and available thin film technologies were used for material deposition. While these approaches offered a significant area gain, the principal disadvantage of the design is the large volume fraction that the substrate occupies. To maximize the energy density, the volume of the substrate should be minimal.

   While most of the proposed geometries are periodic, a 3D-MB can also be constructed from aperiodic structures like foams or aerogels. For example, the so called "sponge" geometry (Figure 2d) has been investigated in a number of studies [8,22,23] where metal or carbon structures are used as a current collector and thereafter coated by electrode material and polymer electrolyte. The counter electrode is formed by filling the remaining pores with suitable materials.

Recently, Johns *et al.* [22] used a carbon aerogel current collector and coated it with MnO_2 and polymer electrolyte layers.

The interdigitated geometry (Figure 2a) proposed by Dunn and co-workers [6,24] also increases the surface area of the electrodes. It makes it possible to correlate the energy density directly to the electrode height and removes the substrate from the cell. However, the height of the pillars will be effectively limited by the resistance of the electrode material. To avoid this effect, interdigitated metal current collectors can instead be covered by the electrode material [25]. In the works of Teixidor, Min, and co-workers [26,27], inter-digitated carbon electrodes and carbon/polypyrrole 3D-MB were produced. The prototype cell [27] only worked for a few cycles due to electrical shorting, but still demonstrated higher gravimetric capacity than electrodeposited thin films.

Generally, materials familiar from conventional Li-batteries [28] are considered to be suitable for 3D-MBs as well. Examples include copper and/or aluminum current collectors, LiCoO2 [29], LiMn2O4 [30], and $LiFePO_4$ [31] as positive electrodes; also V_2O_5 [32] or MnO_2 are possible choices. Graphite is suitable for the negative electrode. Recent studies also include Cu_2Sb or TiO_2 [33] as active materials for the negative electrode [34]. Some systems using solid polymer electrolytes [34,35] have shown promising results.

However, the 3D-MB is still far from a commercial product or even an experimentally working version which can be cycled repeatedly with limited capacity retention. A number of "half cells" (*i.e.,* batteries where experimental anode or cathode is assembled with a Li metal counter electrode for testing) [26,33,36–41] and some experimental "whole cell" batteries have nevertheless been made [15,27,42,43]. While most of the experimental work has demonstrated some clear advantages of the 3D-architectures as compared to conventional electrode structures, most prototype cells have also experienced problems. The interdigitated cell [26,27] was working only for a few cycles before short-circuiting. In [44]a full working 3D-aperiodic battery was demonstrated, but again the cycling stopped after a few cycles.

It can therefore be said that most of the experimental work carried out so far demonstrates "proof of concept" – focused on merely obtaining a working cell or half-cell with 3D-electrodes with limited energy or power density and rate capability [13]. To develop and obtain a 3D-MB for commercial products, a more thorough understanding of the electrochemical processes taking place in the 3D-cell must be obtained. Currently, the most efficient tools for fulfilling this task are computer simulations. Nevertheless, the number of computational studies of the 3D-MB is still very small. The first simulations of 3D-MBs were performed by Hart *et al.* [7] who investigated different electrode arrangements and shapes to evaluate the current density distribution over the electrode surface. They noticed large current density variations over the electrode surface as the arrangement of the electrodes caused a very nonuniform current density distribution. Teixidor *et al.* have investigated the theoretical properties of fractal electrodes [45]. This concept is interesting since it allows an increased surface

area of the electrodes while keeping the volume of the cell constant. Some later theoretical contributions, considering the ionic transport in the electrolyte of the 3D-trench geometry, the discharge dynamics of the trench geometry and the impact of polymer electrolytes on the ionic transport in 3D-interdigitated geometry (Papers **II–V**) are summarized in this thesis.

1.4. Computer simulations and materials modelling

Computer simulations constitute powerful tools to understand and investigate many physical or chemical processes of a wide range. The size of the problems may start at the atomic scale, where the Schrödinger equation is solved, and might end at the cosmological scales, where the evolution of the galaxies are investigated [46]. Similarly, time scales may vary between picoseconds and tens of thousands of years. Simulations allow us to experiment with systems otherwise impossible to study due to geometrical or time restrictions. Furthermore, we can investigate them in a nondestructive ways. We can easily change material and geometrical properties of the system, or make fundamental changes to the chemistry or physics of the system in order to investigate the effects of all sorts of manipulations. Therefore, a computer simulation can be considered a computer experiment. These opportunities make computer simulations a very useful tool to understand the nature of many problems encountered in modern science.

Computer simulations are generally significantly different from the natural phenomena they try to mimic. For example, cellular automaton or Monte Carlo simulations use only a very limited set of rules to model the behavior of often complicated system. A similar reduced complexity is found in agent based simulations, where simulation objects such as consumers, molecules, trees or cells are represented directly and possess an internal state and a set of behavior rules, which in turn determine the agents behavior and modifies it in every simulation time step.

In the theoretical studies of batteries, several levels of simulation can be distinguished. Computational chemistry methods such as Density Functional Theory (DFT) [47], Molecular Mechanics, Molecular Dynamics (MD) [48,49], *ab initio*, *etc*., are useful tools for studying many different problems regarding the chemistry of the battery materials. For example, DFT is generally used to investigate the structural stability of electrode materials. The time scale for DFT-based methods ranges from femto- to picoseconds, while the length scale remains under a couple of nanometers. Thus, the simulations provides very detailed information, but for very limited time and length scales. When larger systems and longer simulation times are of interest, it is possible to use Molecular Dynamics to simulate larger systems of atoms. The range of MD is generally from 20 to 100 nm, while the time scales start from 50 ns and reaches

up to 1 μs (for small systems). Further increase in scale, to the so called meso-scale, facilitates descriptions of material particles or clusters [50]. To characterize the research object at system level, for example the battery during cycling, another tool capable of reaching the necessary time and length scales is needed. To solve these kinds of problems, partial differential equation can be used. In many practical cases where the solution process is numerical, commonly used methods for solving these are the Finite Element Method (FEM) [51–54] or the Finite Difference Method [54,55]. If detailed information about the potential and concentration distribution in the battery is not necessary, equivalent circuit modelling can also be used [56].

1.5. Research objectives

The research object in this thesis is the 3D-microbattery, and the aim of this work is both to provide deeper insights into the ionic transport in these devices and to develop methodology for computer assisted design of 3D-MB geo-metries. This research aim is fulfilled by using computer simulations and the Finite Element Method. The methodology allows simulating complete 3D-structures and all decisive physical and chemical processes in the battery, thereby providing necessary insight to the ionic transport and electrochemical activity in the cell. Theoretical studies of the 3D-MBs should show which 3D-MB designs are viable; point out possible shortcomings in different architectures; give insight and understanding to the ionic transport processes inside the battery; specify how to achieve optimal geometries of the electrode; and show what electrode materials which are optimal. To achieve all these goals, 3D-trench and 3D- interdigitated geometries have been investigated in this thesis through the following steps:

1. Paper **I**: Computer simulations of the ionic transport in the electrolyte of a 2D battery. The starting point of the 3D-MB simulations is established by conducting simulations of a 2D-battery electrolyte. The effect of the separator to the ionic transport in liquid electrolyte is investigated and explained. The main result is the theoretical framework, which enables efficient mass and current balance calculation in the electrolyte at steady state.
2. Paper **II**: Computer simulations of a liquid electrolyte in the 3D-trench geometry. The main properties of ionic transport in the electrolyte of the 3D-trench geometry are investigated. It is identified how the ionic transport in the 3D-MB depends on the electrode conductivity and geometrical details.
3. Paper **III**: Simulation of 3D-MB discharge cycles. Discharge dynamics of the 3D-trench geometry is studied. The effect of the electrode conductivity is investigated; geometrical factors affecting the 3D-MB performance are discovered.

4. Simulations of the 3D-interdigitated geometry. The complexity of the electrode geometry is here increased; different variations of the interdigitated geometry are investigated.
5. Paper **IV**: Simulation of polymer electrolytes in the 3D-interdigitated geometry. The 3D-interdigitated geometry is simulated, and the different effects of using liquid or polymer electrolytes are studied. The cell with polymer electrolyte demonstrated more uniformly distributed electrochemical activity than the cell with liquid electrolyte.
6. Paper **V**: Determination of an optimal 3D geometry by conducting topology optimization of the 3D-trench geometry. Uniform electrochemical activity is achieved by using electrodes with nonuniform electrode material layers. Performance increases above 2 times is achieved as compared to a non-optimized cell.

The provided methodology will help us to understand the electrochemical processes behind the optimal performance of the battery. When the optimum material distribution on the electrode surface is reached, **the experimental techniques of the electrode preparation can be refined or simplified to achieve the best performance of the battery system.**

2. MATHEMATICAL MODELLING OF 3D-MB

2.1. The finite element method

The Finite Element Method (FEM) [51–54] is used to numerically solve second order partial differential equations (PDEs). To use the method, the physical phenomena of interest are identified and expressed as PDEs. Some examples of these equations are the heat equation, Navier-Stokes equation or the diffusion equation. An exact geometrical model of the system, capturing all important geometrical details is thereafter prepared and divided into non-overlapping subdomains (usually referred to as a "mesh"). The PDEs of a mathematical model are approximated with discrete, piece-wise continuous functions, defined in the subdomains of the geometrical model. To find the values of the unknown function, the discrete equations in the subdomains are solved simultaneously. The spatial dimensions of the research object may vary from micrometers to meters, and time-scales from microseconds to hours, sometimes even days.

FEM allows us to simulate processes in the whole battery, and it is the main tool for studying effects which can appear for different electrode geometries and for different material properties.

2.1.1. Mesh

The application of the finite element method starts form the mesh generation, when the geometry is partitioned into small simple subdomains, defined as mesh elements. Mesh elements can vary in size and shape, making it possible to discretize the domain flexibly. For example, the elements can be larger in one part of the simulation area where less accuracy is needed and smaller in regions where high accuracy is needed. In 1D geometries, the mesh is generated by discretizing the domains of different materials to smaller intervals (forming the elements). The endpoints of each element are called vertexes or nodes. The geometry boundaries are represented by boundary elements, formed by the vertices at domain boundaries.

In 2D geometries, usually two types of elements are used – triangular or quadrilateral mesh elements. Unlike 1D problem, the geometrical boundary is often only approximated as curved edges formed by a finite number of elements. It is possible to use a larger number of elements and smaller elements at the curved boundaries to achieve better conformity. Every 2D element consists of vertexes (nodes) at the corners and edges of the elements. The boundaries are represented by the mesh edges lying in the corresponding geometrical boundary and are referred to as boundary or edge elements. If different material domains share a common boundary, the edges and vertexes at the boundary must be conformal.

The geometry of 3D problems can be discretized using tetrahedral, hexahedral, prism or pyramidal mesh elements. Mesh vertexes and edges are defined

as for 1D and 2D problems, while the third dimension adds mesh faces at the sides of the elements. The boundaries of the 3D geometry are divided into triangular or quadrilateral elements. Similar to 2D geometries, faces approximate the geometrical boundary. All faces, edges and vertexes at different material domain boundaries (the internal boundaries) must be conformal.

2.1.2. Finite elements

Once the mesh is generated, the finite element method can be applied. Consider a single variable $u(x)$. This variable must be described with a finite number of parameters, or degrees of freedom. Consider a 1D problem with linear elements and the mesh consisting of two elements, so that $0<x<1$ and $1<x<2$. By using linear elements, the variable u stays linear in each element. In order to express u inside the elements, we need to know its values at the node points $x_1=0$, $x_2=1$, $x_3=2$. Consider these values as $U_1 = u(0)$, $U_2 = u(1)$, $U_3 = u(2)$. These are often denoted as *degrees of freedom*. The value of $u(x)$ can now be expressed in one element as

$$u(x) = \sum_k U_k N_k(x) \tag{1}$$

where $N_k(x)$ are piecewise linear functions; linear in each mesh interval and equal to 1 at the node point k, and 0 in every other node point. The functions $N_k(x)$ are defined as the *basis functions* or shape functions. Obviously, when the variable u is nonlinear, a larger number of elements is needed to capture the nonlinear behavior of u in the total geometry.

2.1.3. Discretization of the equations

Consider the Poisson equation with Neumann boundary conditions, written as:

$$\nabla \cdot \left[\sigma(x)\nabla\phi\right] = f(x) \tag{2}$$

$$\frac{\partial\phi}{\partial\vec{n}} = \gamma(x) \tag{3}$$

If σ is conductivity, ϕ electrical potential and f charge distribution in space, this equation describes electrical current. Then assume a 3D geometry: the simulated volume is denoted Ω with boundaries Γ_i, $i=1,2$, where $i=2$ represents the internal boundary and $i=1$ the external boundary. One possible method to solve Eqs. 2–3 using FEM is to convert them to variational form, achieved by multiplying Eq. 2 with the test function N , followed by integration. The final

version of Eq. 2 is achieved after integration by parts (or application of the divergence theorem):

$$-\underbrace{\int_{\Omega_1} \sigma(x)\nabla\varphi\nabla N(x)dxdydz}_{3} + \underbrace{\int_{\Gamma_2} \sigma_2 \frac{\partial\varphi}{\partial\vec{n}_2} N(x)d\Gamma + \int_{\Gamma_2} \sigma_1 \frac{\partial\varphi}{\partial\vec{n}_1} N(x)d\Gamma}_{2} +$$

$$\underbrace{\int_{\Gamma_1} \sigma_1\gamma(x)N(x)d\Gamma}_{1} = \int_{\Omega} f(x)N(x)dxdydz \qquad (4)$$

where integral 1 describes the boundary condition (Eq. 3), integral 2 the boundary conditions at material interfaces (for example, contact resistance) and integral 3 represents the initial left hand side (LHS) of Eq. 2. If considering continuity boundary condition at the internal boundary, the sum of integral 2 becomes zero.

When using the Galerkin method, the shape function and test function are equal. To discretize Eq. 4, φ is replaced by its approximate value $\varphi = \sum_k N_k^e \Phi_k$,

where k is the node, e an element index and Φ is the calculated value of φ at the node, leading to a final equation in one mesh element:

$$\sum_j \left(-\int_{\Omega} \sigma(x)\nabla N_i N_j dxdydz \right) \Phi_j = \int_{\Omega} f(x)N_i dxdydz - \int_{\Gamma} \sigma(x)\gamma(x)N_i d\Gamma \qquad (5)$$

To solve Eq. 5, the element equations must be combined to a single, global matrix equation. The element equations are assembled to the global equations, for example, as described by Rao [53].

While the Neumann boundary conditions are implemented naturally, constraints such as Dirichlet' boundary conditions must be specified separately. It is possible to include these by using Lagrange multipliers or by manipulating with the finally assembled matrix equation [53].

For practical usage of FEM, large numbers of open source and commercial software packages are available. In the work presented in this thesis, Comsol Multiphysics has been used [57].

2.1.4. Time dependent problem

Comsol Multiphysics can solve time dependent problems using two algorithms. These are generalized-α [58,59] and IDA [60], which bases on DASPK [61] and uses variable order variable step size backward differentiation formulas (BDFs). For a differential equation $y'(t) = f(t, y(t))$, with initial condition $y(t_0) = y_0$,

the simplest implementation of BDF is the backward Euler method, implemented when the time derivative of the function is replaced with the approximation:

$$y'(t) = \frac{y(t) - y(t-h)}{h} \tag{6}$$

This leads to a numerical iterative series:

$$y_{n+1} = y_n + hf(t_{n+1}, y_{n+1}) \tag{7}$$

where h is the time step. Since the time stepping method is implicit, it can lead to a system of nonlinear equations which are to be solved in every iteration step. To manage this problem, Comsol Multiphysics includes a Newton solver in the IDA implementation.

2.2. Mathematical models of the battery systems

To model the electrochemical processes in the 3D-MB, two well-established and experimentally validated mathematical frameworks have been used in this thesis. The first uses dilute solutions and the Nernst-Planck equation [62,63] (Paper **I**), while the second uses concentrated solution theory and Maxwell-Stefan diffusion [64–69]. In literature, it has been argued that concentrated solution theory based methods should be used to model electrochemical processes in Li-batteries, since Li battery electrolytes exhibit concentrated behavior [70]. However, excellent agreement has been demonstrated between experimental result and theoretical predictions using the Nernst-Planck equation for constant current simulations [63]. The full potential of the concentrated solution based models should appear when the battery current is varied or cycled during the simulation, due to considerable concentration fluctuations then appearing in the electrolyte.

In this work, constant current has been used during discharge/charge or at steady state simulations (describing only the electrolyte), thereby making the Nernst-Planck equation approach a relevant tool. The Nernst-Planck equation can be solved efficiently (Paper **I**) at steady state, making it possible to scan large numbers of different 3D-MB geometries for fast evaluation of their performance (in Paper **V**).

The mathematical models used here are based on the following general assumptions:
1. Diffusion constants and conductivities are considered to be constant in the anode, the cathode [65,71] and the electrolyte [63]. An assumption of constant electrolyte conductivity is used only in Papers **II–III**.
2. Side reactions are neglected in the entire cell, leading to a constant total electrolyte concentration.

3. Electroneutrality is assumed in the electrolyte.
4. Volume changes in the electrodes are neglected.
5. Constant transfer coefficients are assumed at all times throughout the electrolyte [68].

The 3D-microbatteries are still a very new field of research, leading to a shortage of experimental data from different experimental 3D-battery designs, not least due to a focus in the scientific community on creating a working prototype or half-cell [13]. As a consequence, the mathematical models used in this thesis are kept as simple as possible to pinpoint the most important ionic transport properties in the 3D-MB systems. For example, the solid electrolyte interface (SEI) layer between the electrodes and electrolyte is not included in the models [65,72,73]. Usually, the layer is inserted as an extra film resistance in the surface overpotential (Eq. 28) [70]. However, currently any experimental information on how the surface resistance is distributed over the experimental 3D-MB electrode does not exist. It is therefore not possible to answers questions like is the film resistance uniform, or is it higher in the more active parts of the electrode. How large are the possible resistance differences? Should only a single SEI resistance value be included, or does the electrode-electrolyte interface resistance consist of both SEI resistance and contact resistance? These details can have serious impacts on the performance of the 3D-MB cell [66,70] and should therefore be addressed in future works when more experimental data is available.

2.2.1. Modelling the electrolyte using the Nernst-Planck equation

If the movement of the solution can be neglected, the driving force of the ionic flux comprises two factors – the chemical and electrical potentials. The first arises from the concentration differences in the solution, while the second originates from the electrical field. Together, they form the electrochemical potential [62]. The ionic flux in the solution can be calculated according to the Nernst-Planck equation, which for a binary electrolyte such as a solution of $LiPF_6$ ($j=Li,PF_6$) can be written for each respective ions as [62]:

$$\vec{J}_j = \vec{J}_j(\mathrm{r},t) = -D_j \nabla c_j(\mathrm{r},t) + \frac{F}{RT} D_j z_j c_j(\mathrm{r},t) \vec{E}(\mathrm{r},t) \qquad (8)$$

where $c_j(\boldsymbol{r},t)$ [mol·m^{-3}] is the ionic concentration, $\boldsymbol{E}(\boldsymbol{r},t) = -\nabla \varphi(\boldsymbol{r},t)$ is the electric field [V·m^{-1}], $\varphi(\boldsymbol{r})$ is the electric potential [V], D_j are the diffusion coefficients [m^2·s^{-1}] and z_j are the valence states ($z_{Li} = -z_{PF_6} = 1$).

In the Li-ion battery, PF_6^- ions cannot penetrate the electrode-electrolyte interface, which leads to an insulation boundary condition for these ions. The boundary condition for the Li^+ flux is [62]:

$$\vec{J}_{Li} = \frac{\vec{j}}{z_{Li}F}, \tag{9}$$

The initial condition for the concentration is $c_{j,0}$= 1500 mol/m^3 for both ions in all simulations.

The concentration change in time can be expressed as a divergence of the ionic flux [62], leading to the following equation system:

$$\frac{\partial c_{Li}}{\partial t} = \nabla \cdot \left(D_{Li} \nabla c_{Li} - \frac{F}{RT} D_{Li} c_{Li} \vec{E} \right) + R \tag{10}$$

$$\vec{n} \cdot \left(D_{Li} \nabla c_{Li} - \frac{F}{RT} D_{Li} c_{Li} \vec{E} \right) \Bigg|_{\vec{r} \in \Gamma} = \frac{\vec{j}(\vec{r},t)}{F} \tag{11}$$

$$c_{Li}(\boldsymbol{r},0) = c_{Li,0} \tag{12}$$

and

$$\frac{\partial c_{PF_6}}{\partial t} = \nabla \cdot \left(D_{PF_6} \nabla c_{PF_6} + \frac{F}{RT} D_{PF_6} c_{PF_6} \vec{E} \right) + R \tag{13}$$

$$\vec{n} \cdot \left(D_{PF_6} \nabla c_{PF_6} + \frac{F}{RT} D_{PF_6} c_{PF_6} \vec{E} \right) \Bigg|_{\vec{r} \in \Gamma} = 0 \tag{14}$$

$$c_{PF_6}(\boldsymbol{r},0) = c_{PF_6,0} \tag{15}$$

Since the electroneutrality is assumed, $c = c_{Li} = c_{PF_6}$, the volume of the electrolyte is considered constant and no side reactions occurs (R=0), the final equation for the mass balance in the electrolyte takes the form (Papers **I**, **IV**, [63]):

$$\frac{\partial c}{\partial t} = D \nabla^2 c \tag{16}$$

$$2D_{Li}\vec{n}\cdot\nabla c = \frac{\vec{n}\cdot\vec{j}}{F} \tag{17}$$

$$c(\boldsymbol{r},0) = c_0 \tag{18}$$

where $D = \dfrac{2D_{Li}D_{PF_6}}{(D_{Li}+D_{PF_6})}$ and $c_0 = c_{Li,0} = c_{PF_6,0}$ is the initial concentration of each ion type.

By using the electroneutrality assumption, subtracting Eqs. 10, 13 and multiplying the result with Faraday's constant F, the following equation for the potential in the electrolyte is achieved:

$$(D_{PF_6}-D_{Li})F\nabla^2 c - \nabla\cdot\left[\frac{F^2 c}{RT}(D_{PF_6}+D_{Li})\nabla\varphi\right] = 0 \tag{19}$$

The boundary conditions are derived by applying the same procedure to Eqs. 11 and 14:

$$\vec{n}\cdot\left[(D_{PF_6}-D_{Li})F\nabla c - \frac{F^2 c}{RT}(D_{PF_6}+D_{Li})\nabla\varphi\right] = \vec{n}\cdot\vec{j} \tag{20}$$

If the ionic conductivity is expressed by the Nernst-Einstein equation $\sigma_{ion} = \dfrac{F^2 c}{RT}(D_{PF_6}+D_{Li})$ and $\vec{j}_{1,2} = (D_{PF_6}-D_{Li})F\nabla c$, Eqs. (19–20) can be re-written in a suitable form for numerical implementation in Comsol Multiphysic's standard conductive media tools:

$$-\nabla\cdot(\sigma_{ion}\nabla\varphi - \vec{j}_{1,2}) = 0 \tag{21}$$

$$-\vec{n}\cdot(\sigma_{ion}\nabla\varphi - \vec{j}_{1,2})\Big|_{r\in\Gamma} = \vec{n}\cdot\vec{j} \tag{22}$$

In the steady state simulations, mass balance in the electrodes is not calculated. Thus, it is possible to simplify the mathematical model and avoid the numerically complicated Butler-Volmer equation (Eq. 28), which significantly increases the computational time and tends to be sensitive to numerical errors. Such an approach becomes possible when the current density distribution in the electrodes is calculated by Ohm's law and uniform concentration in the electrodes is assumed. A constant state of charge raises a uniform potential distribution, which does not affect the current density distribution in the electrodes.

Since the exchange current density in a Li battery system is generally high [74], the charge transport resistance [62] is low and does not affect the current density distribution either. By combining these observations, it is possible to replace the Butler-Volmer equation with the current continuity boundary conditions between the electrodes and electrolyte.

2.2.1.1. Overpotential and the electrical field at steady state

To calculate the electrical field in the electrolyte, the Nernst-Planck equation can be utilized. Consider the ionic concentration at steady state. In this case, the concentration profile is fully developed. The steady state concentration profile is maintained by the Li^+ ion flux through the electrode boundaries. Furthermore, due to the local electroneutrality condition, the concentration of both Li^+ and PF_6^- ions must be equal in every point of the electrolyte. Since the PF_6^- cannot penetrate the electrode boundary, the PF_6^- ions do not contribute to the net current in the electrolyte:

$$\vec{J}_{PF_6}(\mathrm{r}) = -D_{PF_6}\nabla c_{PF_6}(\mathrm{r}) - \frac{F}{RT}D_{PF_6}c_{PF_6}(\mathrm{r})\vec{E}(\mathrm{r}) = 0 \tag{23}$$

which leads to:

$$\vec{E}(r) = -\frac{RT}{F}\frac{\nabla c_{PF_6}(r)}{c_{PF_6}(r)} = -\frac{RT}{F}\nabla \ln c_{PF_6}(r) \tag{24}$$

The electroneutrality condition $c(r,t) = c_{PF_6}(r,t) = c_{PF_6}(r,t)$ leads to the final equation for the electrical field in the electrolyte at steady state:

$$E(r) = -\frac{RT}{F}\nabla \ln c(r) \tag{25}$$

The overpotential in the electrolyte is achieved by integrating Eq. 25 (Paper **I**), leading to

$$\varphi(r_1) - \varphi(r_2) = \int_{r_1}^{r_2} E dr = -\frac{RT}{F}\int_{r_1}^{r_2}\nabla \ln(c)dr = -\frac{RT}{F}\left[\ln(c(r_2)) - \ln(c(r_1))\right] = \frac{RT}{F}\ln(\frac{c(r_1)}{c(r_2)}) \tag{26}$$

Since the diffusion and migration overpotentials in the electrolyte are equal, the total overpotential is calculated by (Paper **I**):

$$\eta = \frac{2RT}{F} \ln \frac{c(r_1)}{c(r_2)} \tag{27}$$

Eq. 25–27 provide a useful tool for solution to the optimization problems in Paper **V**, since they allow the removal of one partial differential equation from the battery simulation setup. This approach becomes especially important when the optimizations are carried out for geometries represented in 3D space, where the demand for computer resources grows fast.

2.2.2. Concentrated solution theory

As said previously, the concentrated solution theory developed by Newman *et al.* is one of the most common methods for modelling the Li battery systems. The ionic transport in the concentrated solution theory is described by Maxwell-Stefan diffusion, which takes not only friction between ions and solvent into account, but also friction between ions of different species [75,76]. It increases the accuracy of the calculations at the cost of increased complexity of the mathematical models.

The electrode kinetics is usually described by the Butler-Volmer equation:

$$j = i_0 \left[\exp\left(\frac{\alpha_a F \eta}{RT} \right) - \exp\left(-\frac{\alpha_c F \eta}{RT} \right) \right] \tag{28}$$

where $\eta = \varphi_s - \varphi_l - V_{oc}$. The open circuit potential is fitted to experimental data for $LiCoO_2$ and for LiC_6 according to Stamps *et al.* [77]. During the charge/discharge simulations, the exchange current density is calculated by:

$$i_0 = F (k_a)^{\alpha_c} (k_c)^{\alpha_c} (c_{s,\max}^j - c_s^j)^{\alpha_c} (c_s^j)^{\alpha_a} (c)^{\alpha_a} \tag{29}$$

where *j=n,p*.

After assuming the electroneutrality, the mass balance for Li^+ and PF_6^- ions in the electrolyte takes the form [65,68,70]:

$$\frac{\partial c}{\partial t} = \nabla \cdot (D \nabla c) \tag{30}$$

where *D* is the diffusion coefficients of the electrolyte.

The boundary condition for Eq. 30 must take into account that the PF_6^- flux over the boundary is zero. It must also be balanced by migration, leading to the following boundary condition [70]:

$$\vec{n} \cdot \nabla c = \frac{j(1 - t_0^+)}{FD} \tag{31}$$

The potential distribution in the electrolyte is calculated by:

$$\nabla \cdot \left(\kappa \nabla \varphi_2 - \frac{2RT}{F}(1 - t_0^+) \kappa \nabla ln(c) \right) = 0 \tag{32}$$

$$\vec{n} \cdot \left(\kappa \nabla \varphi_2 - \frac{2RT}{F}(1 - t_0^+) \kappa \nabla ln(c) \right) = -j \tag{33}$$

where κ is the ionic conductivity. To calculate the ionic conductivity, the Nernst-Einstein equation was used by Wang *et al.* [72]. Although the authors noted inaccuracies in the Nernst-Einstein equation for polymer electrolytes, a good agreement between experiment and simulation predictions was achieved.

2.2.3. Potential and concentration in the electrodes

The potential in the electrodes (φ_1) is calculated according to:

$$\nabla \cdot (\sigma_i \nabla \varphi_1) = 0, \ i = 1,3 \tag{34}$$

$$\vec{n} \cdot (\sigma_i \nabla \varphi_1) = j \tag{35}$$

The boundary condition at the positive current collector specifies the battery current

$$\vec{n} \cdot (\sigma_1 \nabla \varphi_1) = -j_0 \tag{36}$$

where j_0 [A/m^2] is charging or discharging current. In the negative current collector, the zero potential is used as boundary condition.

The material balance in the electrodes is described by the diffusion equation [65,68,70]:

$$\frac{\partial c_s}{\partial t} = \nabla \cdot \left(D_{Li}^* \nabla c_s \right) \tag{37}$$

$$\vec{n} \cdot \nabla c_s = \frac{-j}{FD^*{}_{Li}} \qquad (38)$$

where $D_{Li}{}^*$ is diffusion coefficient of lithium in the electrode material. For the electrode-electrolyte interface, the lithium flux boundary condition (Eq. 38) is used, and for the other electrode boundaries, insulation conditions are applied.

2.3. Optimization of the battery electrodes

2.3.1. Optimization strategies

The optimization of the 3D-MB geometry could be carried out by three different strategies. The first is to parameterize the geometry, and thereafter change the parameters during the simulations to finally conclude the optimal set of parameters. An obvious drawback of such an approach is that a very large number of simulations are needed, and it will therefore be computationally expensive to determine the best result. A second possible strategy is to use a parameterized geometry, but select the optimal configuration by some optimization routine. Gradient based optimization methods [78,79] cannot be used, since the parameterization of the geometry changes the mesh during the calculations. This introduces random numerical noise into the objective function and ultimately terminates the calculations. The only way to follow this strategy would be to use stochastic optimization methods such as genetic algorithms [80] or simulated annealing [81], *etc.* The drawback of these methods is the large number of iterations needed to reach the optimal solution.

A third strategy is to use structure topology optimization methods [82], where the optimal geometry is calculated directly by manipulation of the material properties. In the homogenization methods, for example the SIMP (Solid Isotropic Material With Penalization) method [83,84], artificial material is introduced and its porosity is varied between 1 and 0, while intermediate values are penalized using power functions. This method is fairly simple to implement [85], but its main shortcoming is its ability to introduce material with spatially variable porosity [82]. A second shortcoming arises during battery geometry optimization, since the methodology incorporates an ability to generate structures with internal holes. Initial experiments using this method demonstrated this effect. Thus, region based optimization methods, where the electrode shape is altered during the optimization, would be preferential. One such example used here is the level set method [86–88]. These geometry optimization methods are most often used to solve problems in structural mechanics [82], however, the level set method has also been used to solve two phase flow fluid dynamics problems [89,90], heat transfer problems [91] and electromechanical problems – Luo *et al.* for example optimized the shape of an

electromechanical actuator [92]. The homogenization methods have been effectively used to solve different (multi)physics problems [93–95].

Although the structural topology optimization methods have been developed to solve structural mechanics problems, they can be extended to battery modelling, since the structure of the equations in these problems is similar. For example, the stress-strain relationship can be written as [52,53]:

$$-\nabla \cdot \sigma = F \tag{39}$$

where $\sigma=D\varepsilon$ is the stress tensor, where D is a 6×6 elasticity matrix and ε is strain. The theory describing the optimization with the level-set methods [87] is general and without any restrictions to the material parameters. If we then consider the Poisson ratio to be zero and the deformation components u, v, w to be independent of each other, which leads to $U=u+v+w$ and $\partial U/\partial x=\partial u/\partial x$, $\partial U/\partial y=\partial v/\partial y$ and $\partial U/\partial z=\partial w/\partial z$, Eq. 39 simplifies to:

$$-\nabla \cdot E\nabla U = F \tag{40}$$

where E is the modulus of elasticity. The structure of Eqs. 40, 16 and 21 coincides at steady state; the only differences can be found in the physical nature of the material parameters such as modulus of elasticity, conductivity or diffusivity.

Porous electrodes are used during battery optimization with the level set method to make the system less sensitive to the numerical errors. Material boundaries, expressed through the level set method, can move through the mesh elements, producing very high peak values in the potential [88] which, in turn, can lead to a premature end of the simulations due to large numerical errors.

2.3.2. The objective function

To evaluate the battery geometry quantitatively, a function to be minimized (or maximized) is needed. This function is in optimization theories called the objective function. The goal of the optimization of the 3D-MB geometry is here formulated as the achievement of as uniform material utilization as possible in the cell. This is reached by designing a cell with as uniform current density as possible over the electrode-electrolyte interface. By using this approach, it becomes possible to find both maximum current and maximum material utilization.

The first step towards formulating the objective function is to derive it at the level of the entire 3D-MB geometry. It is assumed that the 3D-MB geometry is optimal when the (average) current density vector components in x-, y-, z-directions in the battery are equal. This should mean that the battery geometry utilizes all advantages of the 3D-geometry.

The optimization of the 3D-MB is divided into two steps:

1. In the first step of the optimization, a suitable objective function is constructed to be used as an indicator during the evaluation of different 3D-MB geometries. During this stage, the 3D-MB geometry is studied by parametric simulations, where different geometrical parameters – pillar/plate height, their distance, *etc.* – are changed.
2. In the second step, structural topology optimization is used to calculate the optimal 3D-MB geometry.

The starting point is to calculate the average current density (or ionic fluxes) in all directions. The current density incorporates diffusive and migrative fluxes and the conductivity of the electrolyte, thereby providing an accurate description of the battery electrolyte:

$$\bar{j}_i = \frac{1}{V} \int_\Omega \sqrt{j^2_i} \, d\Omega, \qquad i = x, y, z \tag{41}$$

Thereafter, every average current density component is normalized:

$$\bar{J}_i = \frac{3\bar{j}_i}{\bar{j}_x + \bar{j}_y + \bar{j}_z} \qquad i = x, y, z \tag{42}$$

According to Eq. 42, normalization of the average current density vector components in an ideal geometry, where the average current density in all directions is equal, should result in that every component would be 1.

The final objective function is constructed as a vector relative to an ideal current density distribution, such that $\vec{R} = \vec{J}_{ideal} - \vec{J}$, $\vec{J}_{ideal} = (1,1,1)$. The vector $\vec{R}$ shows the direction towards an optimal geometry, and its magnitude is equivalent to the relative distance between the optimal and the current geometry. If $R=0$, an optimal geometry is achieved:

$$R = \sqrt{(1 - \bar{J}_x)^2 + (1 - \bar{J}_y)^2 + (1 - \bar{J}_z)^2} \tag{43}$$

To calculate the maximum value of R, it can be useful to consider the worst possible ionic transport scenario can be considered: the current is moving only in one spatial direction (corresponding to the transport direction in a conventional 2D battery). In this case, Eq. 42 results in $J_x=3$ and $J_y=J_z=0$. Insertion to Eq. 43 then leads to $R = \sqrt{6} \approx 2.45$.

During the structural topology optimization of the 3D-MB geometry, it is necessary to modify the objective function, since its spatial distribution is vital

for the calculations. The cost function can be further simplified, since it is known that the location of the optimal solution is independent of any constant added to the objective function. So, instead of using $\vec{R} = \vec{J}_{ideal} - \vec{J}$, the magnitude of the current density can be used:

$$F = \int_{\Omega} \sqrt{j_x^2 + j_y^2 + j_z^2}\, d\Omega \tag{44}$$

A similar approach was used by Zhuang *et al.* [91], who used quadratic heat flux as an objective function to solve heat transport optimization problems.

2.3.3. The level set method

It the level set method, the material boundary is represented by a zero level-set of some higher dimensional function in the design domain [86,87]. The distribution of material, depending on the level-set function, is illustrated in Figure 3 where $\phi(x)>0$ corresponds to region 1, $\phi(x)<0$ corresponds to region 2 and $\phi(x)=0$ corresponds to the material boundary:

$$\phi(x) > 0, x \in \Omega_1 \text{ (region 1)}$$
$$\phi(x) = 0, x \in \partial\Omega \text{ (region boundary)} \tag{45}$$
$$\phi(x) < 0, x \in \Omega_2 \text{ (region 2)}$$

The regions with different materials are defined by using the Heaviside function:

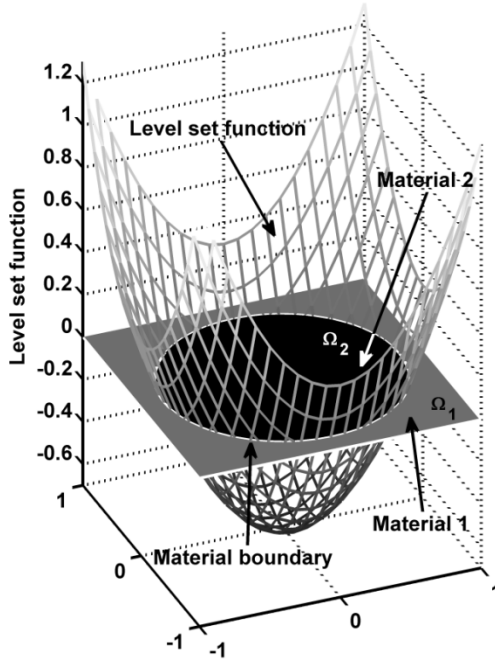$$H(\phi) = \begin{cases} 1, \phi \geq 0 \\ 0, \phi < 0 \end{cases} \tag{46}$$

Figure 3. Material properties and geometry regions expressed through the level-set function. The zero level set represents the material boundary and divides the region into two sub-regions with different material.

In practical applications, a smoothed Heaviside function is used to avoid numerical problems at the region interfaces.

To express the boundaries of the regions, the level-set function dependent Dirac delta function is used:

$$\delta(x) = \frac{dH}{dx} = \nabla H \cdot \frac{\nabla \phi}{|\nabla \phi|} = \delta(\phi)|\nabla \phi| \qquad (47)$$

The normal vector of the level-set surface boundary is calculated as:

$$\vec{n} = \nabla \phi / |\nabla \phi| \qquad (48)$$

The level-set function is a Hamilton-Jacoby type equation and is usually expressed as:

$$\frac{\partial \phi}{\partial t} + V_n |\nabla \phi| = 0 \qquad (49)$$

where V_n is the normal velocity of the moving domain boundaries in the system. The numerical solution of the level-set equation is carried out in the CFT Toolbox in Comsol Multiphysics. There, the solution of the level set equation is implemented according to Olsson *et al.* [89,90]:

$$\frac{\partial \phi}{\partial t} + \vec{u} \cdot \nabla \phi = \gamma \nabla \cdot \left(\varepsilon_{ls} \nabla \phi - \phi(1-\phi) \frac{\nabla \phi}{|\nabla \phi|} \right) \qquad (50)$$

The LHS of Eq. 50 describes the evolution of the level-set function while the right hand side (RHS) guarantees the numerical stability. In the simulations presented here, one of the main differences from previous work is that a 0.5 level-set is used instead of a zero level set. However, Eq. 50 includes methods for reinitialization to guarantee the numerical accuracy of the calculations. In Eq. 50, $\vec{u}=\vec{u}(x,y)$ is the velocity of the level-set surface. However, for the solution of the optimization problem, the normal directional velocity is needed – and this is a quantity with a scalar value. On the other hand, the velocity of the level set surface can easily be expressed through the normal velocity and the normal vector of the surface. Since there are no restrictions for $\vec{u}$, it can be expressed as $\vec{u} = V_n \cdot \vec{n} = V_n \cdot \dfrac{\nabla \phi}{|\nabla \phi|}$. Now, the $\vec{u} \cdot \nabla \phi$ term in Eq. 50 can be replaced with the relation:

$$\vec{u} \cdot \nabla \phi = V_n \frac{\nabla \phi}{|\nabla \phi|} \cdot \nabla \phi = V_n \frac{|\nabla \phi|^2}{|\nabla \phi|} = V_n |\nabla \phi| \qquad (51)$$

When inserting Eq. 51 into Eq. 50 the following equation is obtained, and is to be solved during the optimization of the battery geometry:

$$\frac{\partial \phi}{\partial \tau} + V_n |\nabla \phi| = \gamma \nabla \cdot \left(\varepsilon_{ls} \nabla \phi - \phi(1-\phi) \frac{\nabla \phi}{|\nabla \phi|} \right). \qquad (52)$$

In Eq. 52, the left hand side is identical to Eq. 49 and describes the movement of the level set surface. The expression on the right hand side guarantees the numerical stability and reinitialization of the level set surface. Pseudo time τ, reflecting the optimization iterations, is used instead of time, as the optimization problem is solved with the time dependent solver. The battery model is stationary in every optimization step (Paper **V**).

2.3.4. Battery modelling during the optimization

To carry out the battery modelling, its geometry must be expressed through the level-set function. This can be done by using a combination of material parameters, the level-set function and the Heaviside function [87,88]. The spatial distribution of the conductivity of the electrolyte consists of two parts: the conductivity of the electrolyte in the composite porous electrodes [65,70] and the conductivity of the electrolyte outside the porous electrodes. The spatial distribution of the conductivity is established using the Heaviside function:

$$\sigma_l(\phi) = \varepsilon^{1.5}\sigma_l \cdot H(\phi) + \sigma_l \cdot (1 - H(\phi)) \tag{53}$$

The first term at the right hand side represents the electrolyte conductivity in the porous electrodes and the second the conductivity of the electrolyte.

The electronic conductivity of the electrode material is calculated by the following equation:

$$\sigma_s(\phi) = (1 - \varepsilon)^{1.5}\sigma_j \cdot H(\phi) + \sigma_0 \cdot (1 - H(\phi)) \text{ , } j\text{=}n,\, p \tag{54}$$

where j=n corresponds to the negative and j=p corresponds to the positive electrode. The total electronic conductivity of the battery electrodes consists of the conductivity of the porous electrode (first term at the right hand side) [65,70] and an "artificial" conductivity in the electrolyte area. This artificial conductivity σ_0 has a very small numerical value, but must be used to avoid numerical singularities. It is a standard technique used in structural topology optimization [82].

Similarly to the conductivity, the diffusion coefficient of the electrolyte species consists of two components: the porous electrode [65,70] and the electrolyte. The diffusion coefficient is expressed through the level set function in the following equation:

$$D_i(\phi) = \varepsilon^{0.5}D_i \cdot H(\phi) + D_i \cdot (1 - H(\phi)) \text{ , } i\text{=}Li,\, PF_6 \tag{55}$$

To calculate the flux of species i, the Nernst-Planck equation is used. All material parameters in the Nernst-Planck equation are expressed through the level-set function. Since electroneutrality is assumed, $c = c_{Li} = c_{PF_6}$, and the final equation for calculating the concentration profile is (Paper **V**):

$$\frac{2D_{Li}(\phi)D_{PF_6}(\phi)}{(D_{Li}(\phi) + D_{PF_6}(\phi))}\nabla^2 c = -\frac{1 - t_+^0}{F}a_s j \tag{56}$$

Since porous electrodes are used, insulation boundary conditions are applied for Eq. 56; the Li$^+$ flux is described through the source term at the right hand side of Eq. 56 [64,65]:

$$\frac{2D_{Li}(\phi)D_{PF_6}(\phi)}{(D_{Li}(\phi) + D_{PF_6}(\phi))} \vec{n} \cdot \nabla c = 0 \tag{57}$$

The calculation of the potential is modified similarly to Eq. 56 by adding the insulation boundary condition and the source term to the right hand side of Eq. 19 (see Paper **V**):

$$(D_{PF_6}(\phi) - D_{Li}(\phi))F\nabla^2 c - \nabla \cdot \left[\frac{F^2 c}{RT}(D_{PF_6}(\phi) + D_{Li}(\phi))\nabla\varphi\right] = a_s j \tag{58}$$

The current density in the electrodes and current collectors takes the form of:

$$\nabla \cdot \sigma_i(\phi)\nabla\varphi = a_s j \text{ , } i\text{=}Al,\ p,\ n,\ Cu \tag{59}$$

The boundary conditions for the Eq. 59 are Eq. 36 in the positive current collector, zero potential in the negative current collector and insulation at the electrode-electrolyte interface. In Eqs. 56–59, a_s is the specific surface area [68].

To achieve convergence at steady state, an extra constraint must be specified to guarantee mass balance (Paper **IV**):

$$\frac{1}{V}\left(\int_\Omega c\,d\Omega - \int_\Omega c_0\,d\Omega\right) = 0 \tag{60}$$

2.3.5. The general optimization problem

To obtain an optimal geometry for the 3D-MB, the cost function must be minimized. During this procedure, the volume of the electrodes must be monitored and the amount of active material in them must be maintained. If not, the optimization routine may fill the entire battery with electrode or electrolyte material. By using the objective function (Eq. 44), the general optimization problem of the 3D-MB topology optimization can be written as:

$$\text{Minimize } \quad J(\phi) = \int_\Omega F\,d\Omega = \int_\Omega \sqrt{j_x^2 + j_y^2 + j_z^2}\,d\Omega \tag{61}$$

$$\text{Subject to} \int_{\Omega} H(\phi)d\Omega = V^*$$

where V^* is the volume of the electrodes, F is the objective function and J is the integral to be minimized. The objective function is calculated by solving the Nernst-Planck equation, as presented in previous section.

In the implementation of the optimization routine, method of Lagrange multipliers is used according to Wang *et al.* [87]. This leads to the following equation for the speed function V_n:

$$V_n = (F + \lambda)\delta(\phi) \tag{62}$$

The speed function is used instead of normal velocity to reflect its dependence on the level set function and cost function. According to Eqs. 49, 52 and 62, the shape evolution of the level set surface can be calculated as:

$$\frac{\partial \phi}{\partial \tau} + (F + \lambda)\delta(\phi)|\phi| = \gamma \nabla \cdot \left(\varepsilon_{ls} \nabla \phi - \phi(1 - \phi)\frac{\nabla \phi}{|\nabla \phi|} \right) \tag{63}$$

Here, τ represents the pseudo time passed during one optimization step, since a time-dependent solver must be used to obtain a solution for Eq. 63 which will converge to the initial condition dependent local minimum. The solution of the optimization problem will be terminated when following condition is fulfilled [87]:

$$\int |V_n|\delta(\phi)|\nabla \phi|d\Omega \leq \gamma_{tol} \tag{64}$$

where γ_{tol} is the specified error limit. The Lagrange multiplier, keeping the electrode area constant is calculated according to [87]:

$$\lambda = \frac{\int_{\Omega} F_0 \delta^2(\phi)|\phi|d\Omega}{\int_{\Omega} \delta^2(\phi)|\phi|d\Omega} \tag{65}$$

2.3.6. Cell performance

Using the methodology described above, both, the optimal and a nonoptimal cell would have approximately the same theoretical capacity, the same footprint area, and similar geometries. The most distinctive difference will appear in the distribution of active material in the electrode layers. These similarities make
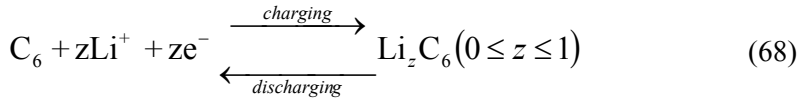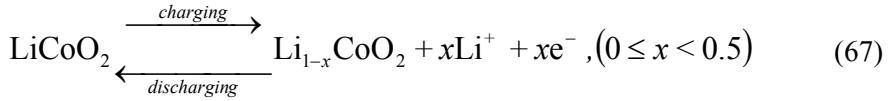
quantitative comparisons complicated, since the cells will act rather similarly during the discharging process due to their equivalent capacities. Therefore, to evaluate the effect of optimization, the energy spent on charge transport is calculated and compared in both geometries using a specific *performance gain* (Paper **V**):

$$\frac{P_{nonopt}}{P_{opt}} = \frac{j_0^{\;2} \cdot r_{nonopt}}{j_0^{\;2} \cdot r_{opt}} = \frac{r_{nonopt}}{r_{opt}} \tag{66}$$

Here, j_0 is the current density, r_{opt} is the resistance of the optimized cell and r_{nonopt} is the resistance of the reference cell. The performance gain characterizes the power gain, relative to the nonoptimal geometry, due to the optimization.

2.4. Simulated 3D-MBs

The materials used in these studies of 3D-MBs are all common macroscopic 2D-battery materials. $LiCoO_2$ has consequently been used as positive electrode material, while LiC_6 (lithiated graphite) has been used as negative electrode material [77,96]. The electrolytes used in the simulations are either a $LiPF_6 \cdot PEO_{20}$ polymer electrolyte or 1.5 M $LiPF_6$ dissolved in a mixture of ethylene carbonate and diethylene carbonate liquid solvents [97]. The electrochemical reactions in the electrodes are:

$$LiCoO_2 \xrightleftharpoons[discharging]{charging} Li_{1-x}CoO_2 + xLi^+ + xe^- , \left(0 \le x < 0.5\right) \tag{67}$$

$$C_6 + zLi^+ + ze^- \xrightleftharpoons[discharging]{charging} Li_zC_6 \left(0 \le z \le 1\right) \tag{68}$$

The simulated geometries treated in this thesis are the "3D-trench" and "3D-interdigitated" architectures (see Fig. 2). The 3D-trench geometry can be seen as a starting point for the simulations, primarily due to its symmetry. It is possible to model it using 2D-simulations, and thereafter extend the results to a 3D system. Moreover, the 3D-trench geometry can be treated as a simplified model of both the 3D-interdigitated and 3D-concentric geometries. A model of the 3D-interdigitated geometry is achieved by selecting a "plate" from both electrodes and rotating them separately around their axis, leading to a series of cylinders attached to the electrode bases. Similarly, a model of the 3D-concentric geometry is achieved when a plate is selected from both electrodes and their combination is rotated around the axis of one plate, thereby building a

cylinder on one electrode which is surrounded by cylinders of first electrolyte and then the counter electrode. The simulations of the trench geometry can therefore provide important and detailed information and valuable insights about three 3D-MB geometries; indeed making it a very versatile tool.
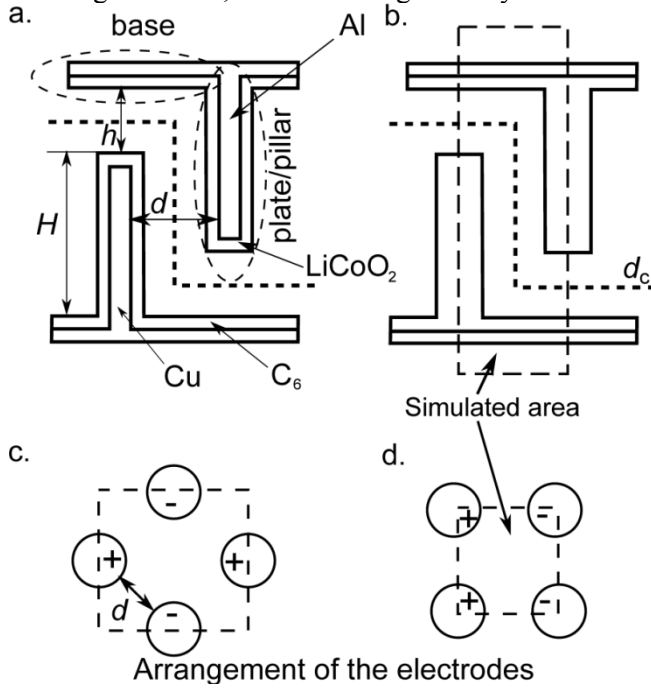

Figure 4. Schematics of the simulated 3D-battery systems.

The geometries of the 3D-MBs discussed in this thesis are summarized in Fig. 4. Fig. 4a shows a cross section of the trench or the interdigitated geometry where conformal active material layers are covering the current collectors. Since the current collector plates or pillars build up the electrodes together with the active material, they can be considered composite electrodes. Fig. 4b shows a cross section of the trench model, where the entire 3D-electrode structure is built up solely of active material. Fig. 4c-d show different pillar arrangements used for the interdigitated geometry. Generally, all 3D-MBs considered in the simulations are interdigitated micro-scale plate or pillar arrangements consisting of 20–100 μm long (H) active material coated Cu and Al current collector plates/pillars with generic parameters, specified in Appendix I.

3. RESULTS

3.1. Basic characteristics of ionic transport in the 3D-MB systems

The development of the concentration distribution in a conventional 2D-battery during discharge is presented in Figure 5. The simulated cell contains a liquid electrolyte and a separator, which is represented as a thin ionically non-conductive layer in the middle of the electrolyte (Paper **I**). The concentration distribution near the electrodes starts to change uniformly since the current density distribution over the electrode surface is uniform. The concentration increases near the negative electrode (x=0) where Li^+ ions are deintercalated and inserted into the electrolyte and decreases at the positive electrode where Li^+ is intercalated into the positive electrode (x=2.8·10^{-4}m). The concentration profile at steady state is linear, except in the middle of the electrolyte where the separator membrane affects the ionic flux.
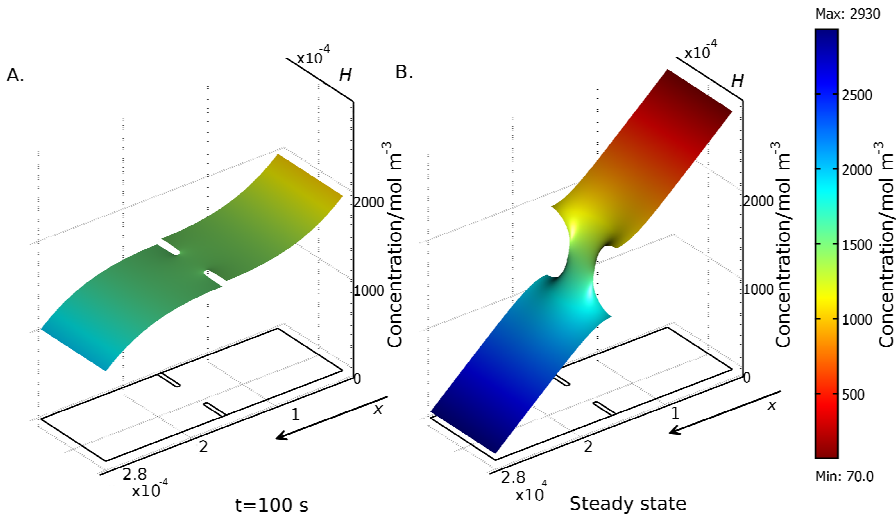

Figure 5. Concentration profile development in a conventional battery electrolyte-separator system.

The concentration distribution in the electrolyte changes radically when 3D-electrodes are utilized (Paper **II**). For example, the concentration distribution development in the electrolyte of the trench geometry is illustrated in Figure 6. The initially uniform concentration distribution starts to change due to the discharging current, primarily near the tip of the negative electrode where the concentration increases rapidly. The development of the concentration profile continues at the base of the positive electrode, where concentration

decreases. Finally, the concentration profile stabilizes; however, the most significant changes appear near the tip of the negative electrode. The concentration distribution in the electrolyte is non-linear due to the inhomogeneous current density. The electrodes have different conductivities, just as in a conventional 2D geometry, but in 3D the arrangement of electrode material affects the current density distribution – most of the current is moving through the tip of the negative electrode (which has higher conductivity) to the base of the positive electrode.
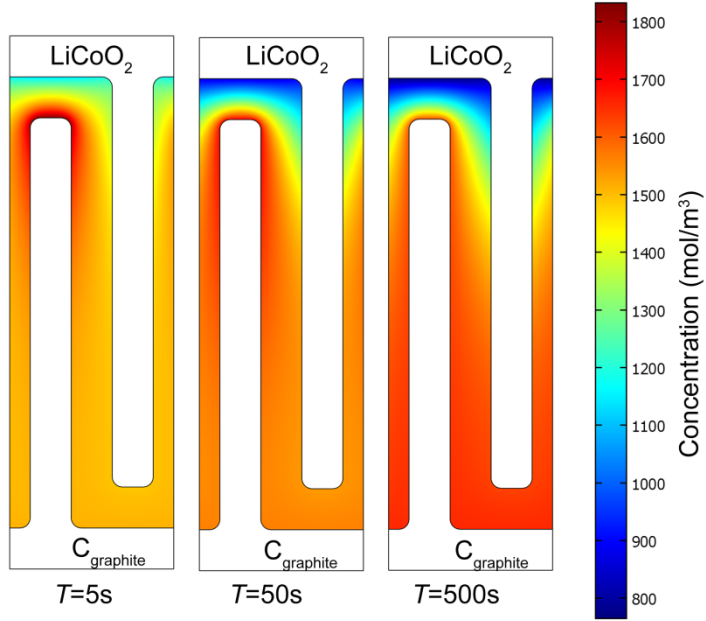
Figure 6. Li$^+$ concentration profile development during discharge in the 3D-trench geometry.

The concentration distribution in the electrodes during discharge is presented in Figure 7. The nonuniform current density distribution in the cell is reflected by nonuniform material utilization in the electrodes. The material depletion in the negative electrode is fastest at its tip, since the current density there is the highest (Paper **III**).

The simulation results demonstrate some distinctive disadvantages of the 3D battery construction as compared to 2D geometries. A simple construction of a 3D geometry suppresses the full potential of the 3D-architectures due to the nonuniform current density originating in the conductivity differences between the electrodes. As a result, the high electrode surface area in the 3D-architecture is not utilized, but reduced to an *effective surface area* with a size equal to the tip of the negative electrode. Thus, the maximum current which a simple

3D-battery can deliver is significantly reduced and it reaches its limiting current fast. To operate 3D electrodes effectively, the whole surface area of the electrode must be utilized. Different strategies to achieve this effect are discussed in the following text.
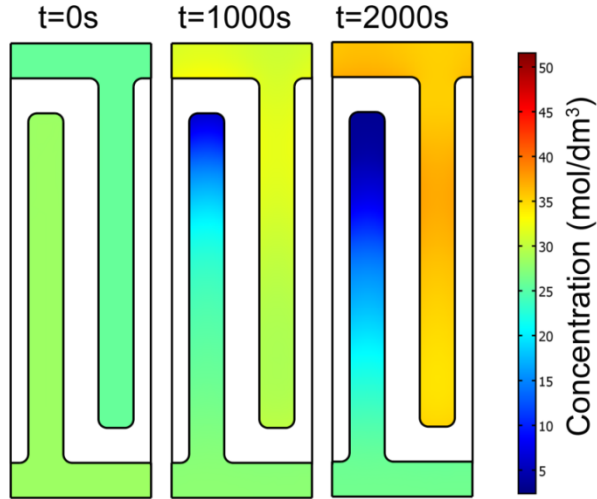

Figure 7. Concentration profile development in the 3D-trench geometry during discharge. Top electrode: $LiCoO_2$ (0.01 S/m). Bottom electrode: LiC_6 (1 S/m).

3.2. Impact of electrode materials

The first step in the investigation of methods for increasing the uniform material utilization in the 3D-MB is studying the effects of the electrode material properties by altering its electronic conductivity. As discussed above, it was the difference in electronic conductivity which gave rise to inhomogeneities. In Figure 8, the concentration gradient in the electrolyte at steady state is presented for different positive electrode conductivity values. During the simulations, the conductivity of the positive electrode ($LiCoO_2$) was gradually increased from 0.01 S/m to 1 S/m, until it was equal to the conductivity of the negative electrode (LiC_6). Experimentally, this effect could be achieved by adding electronically conductive additives to the positive electrode.

The electrochemical activity on the electrode surfaces has been evaluated by using the concentration gradient of the ions, which is proportional to the current moving through the battery (Paper **II**). To find the maximum utilization of electrode material, electrode parameter configurations have been searched so that the differences in concentration gradient on the electrode surface have been minimal. The concentration gradient for σ=0.01 S/m corresponds to the concentration profile in Figure 6. The concentration gradient is at its maximum at

the tip of the negative electrode, indicating that almost all electrochemical activity is concentrated to this region. The concentration gradient then drops fast when moving towards the base of the negative electrode. One way to optimize the material usage of the 3D-MB is therefore to decrease the height of the pillars or plates, which are the characteristic features significant for the 3D-electrode. However, some vital advantages of the 3D geometry – a high surface area gain and increased capacity – are lost if using this strategy (Paper **II**).

When the conductivity of the positive electrode is increased, the concentration gradient in the electrolyte becomes gradually more uniform and finally an almost constant distribution develops when the electrode conductivities are equal. Only the tips of the electrodes are then affecting the concentration gradient. By choosing electrodes with equal conductivities, a uniform concentration gradient in the electrolyte is achieved, since all possible routes for the current become equally favorable. Only the sharp electrode tips, where the electrical field is nonuniform, produce a nonuniform concentration gradient (Paper **II**).
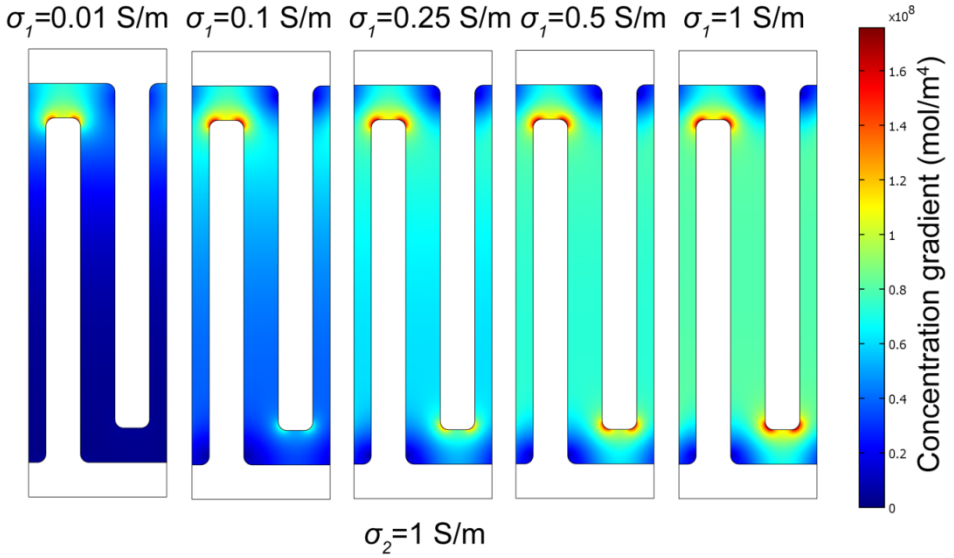

Figure 8. Steady state concentration gradient distribution dependence of the cathode conductivity (σ_1). The anode (σ_2) has constant conductivity.

The concentration distribution in the electrodes of the 3D-trench geometry having equal conductivity in the positive and negative electrode is presented in Figure 9. Although the concentration gradient is rather uniform due to the equal conductivities, the utilization of the electrode material is still nonuniform. The tips of the electrodes are delithiated/lithiated first when the discharging process

continues from the plate tip towards the base. Nonuniform delithiation/lithiation of the electrodes terminates the discharging process prematurely when approximately 80 % of the theoretical capacity is utilized.

Thus, even with the most favorable electrode conductivity configuration, a uniform material utilization in the electrodes cannot be guaranteed. This problem appears due to the very geometry of the electrodes. The surface area and amount of active material is much larger around the electrode base area than around the opposing electrode tip. This leads to a much higher local current density in the electrode tip than in the opposing electrode base, causing inhomogeneous material utilization in these regions. The problem could be solved by using a different geometry, for example 3D-concentric (Fig. 2c), or by using electrodes with nonuniform material layer thickness (Paper **III**).
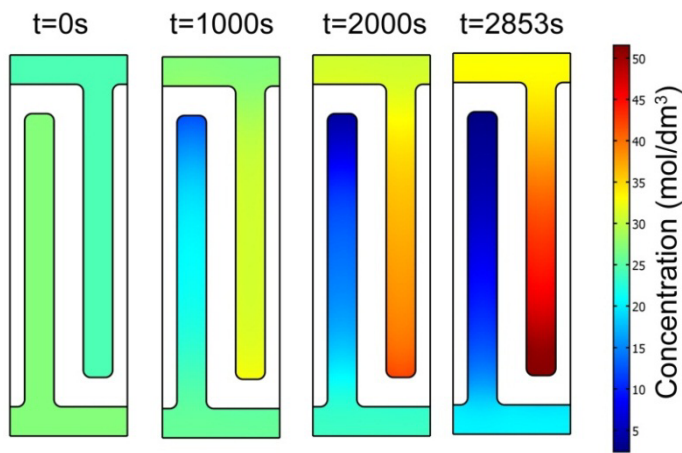

Figure 9. Concentration profile development in the 3D-trench geometry during discharge. Top electrode ($LiCoO_2$), and bottom electrode (LiC_6) have equal conductivity (1 S/m).

The effect of the electrode conductivity on the cell voltage is presented in Figure 10 where the discharge curves for different positive electrode conductivity values are presented as a function of x in Li_xCoO_2. In all calculations, the same discharge current density ($J=18$ A/m^2) is used. When the positive electrode has a realistic conductivity value (0.01 S/m), the cell voltage reflects the nonuniform material utilization effects, described in Figs 7–9, and therefore demonstrates high concentration polarization. It leads to a premature end of discharge, and the cutoff voltage (3.5 V) is reached at $Li_{0.67}CoO_2$. When the conductivity of the positive electrode is increased, a more homogenous material utilization is achieved (Figs. 8–9) and the concentration polarization is significantly reduced. The cell voltages almost coincide if the positive electrode conductivity is larger than 0.25 S/m. This clearly demonstrates the crucial effect

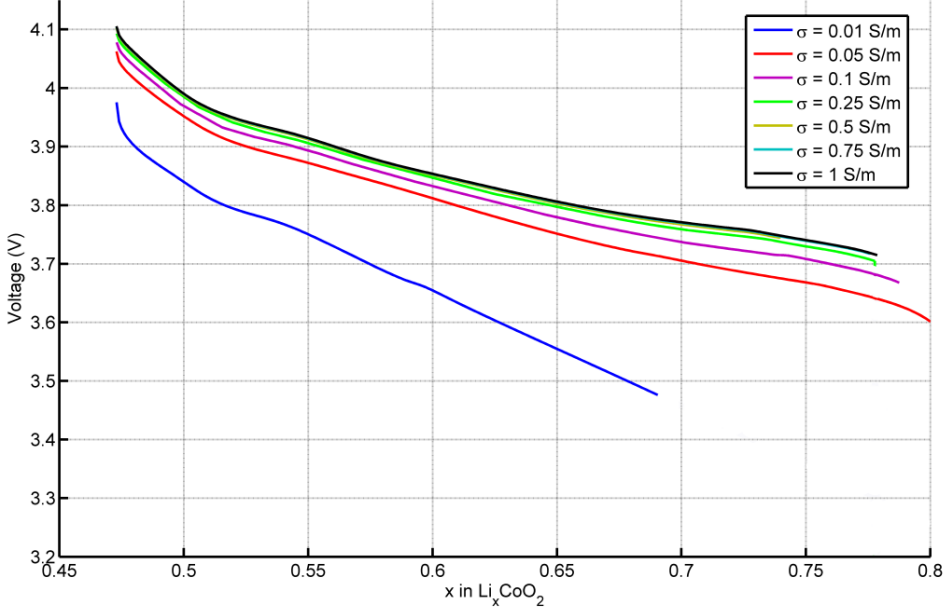of homogenized electrode conductivities in order to obtain a 3D-MB with maximum performance.

Figure 10. Discharge curves of the 3D-trench microbattery for different positive electrode conductivity values. Discharge curves at σ = 0.5, 0.75 and 1 S/m are overlapping. The discharging current density was 18 A/m^2.

3.3. 3D-MB geometry optimization by redistribution of electrode material

As discussed above, one of the key strategies for optimizing the 3D-MB performance, equalization of the electrode conductivities, could be achieved by increasing the positive electrode conductivity or decreasing the negative electrode conductivity. This goal could also be achieved by using electrode additives or porous electrodes. However, the obvious shortcoming of a decreased negative electrode conductivity is a reduced battery current, while porous electrodes will decrease the capacity. Nevertheless, one possible method to increase the average conductivity of the electrodes is to use 3D metal current collectors and coat them with the electrode layer. Such a configuration is presented in Figure 11, where electrodes with different conductivities are compared with electrodes consisting of active material coated onto 3D current collectors [98]. The battery with "composite" electrodes displays an almost uniform concentration gradient distribution, similar to the system with uniform conductivities.

This uniform concentration gradient distribution is achieved because the metal current collectors in the electrodes have very high conductivity values and act as equipotential surfaces in the electrodes. Thus, the potential is always constant in the center of the electrode pillars/plates and the current moves almost straight between the electrodes.
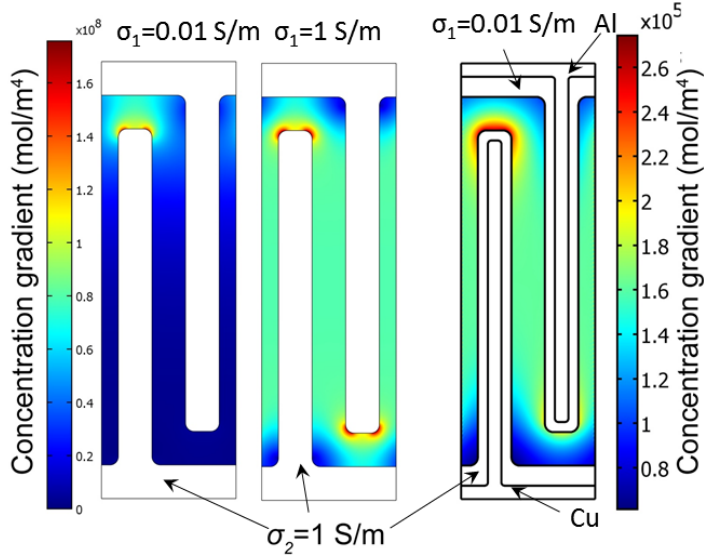

Figure 11. Concentration gradient in the trench geometry with and without the current collectors in the plates

The concentration gradient and electrochemical activity in the 3D-MB does not only depend on the electronic conductivity of the electrodes, but also on the electrode shape. Also equal positive and negative electrode conductivity values leads to nonuniform concentration gradients near all corners in the architecture, as demonstrated in Figure 8 and Figure 11. This effect can be decreased by rounding the sharp tips, so that the electrochemical activity will be distributed over the whole surface area of the electrode tips. This is illustrated in Figure12, where the effects of different extreme electrode corner radiuses of curvatures are presented. The sharp corners at the electrode tips, where the electrical field (and current density) becomes very large, increase the concentration gradient and leads to a high local current density in the respective areas. This may result in unwanted side reactions which can damage the electrode material. By using round electrode tips, the maximum concentration gradient is decreased and the concentration gradient is distributed more evenly over the entire electrode surface, leading to more uniform material utilization (Paper **II**). It can be concluded from Figure 12 that redistribution of active material in certain parts of the electrodes can be a useful tool to achieve a more uniform electrochemical activity in the 3D-MB.
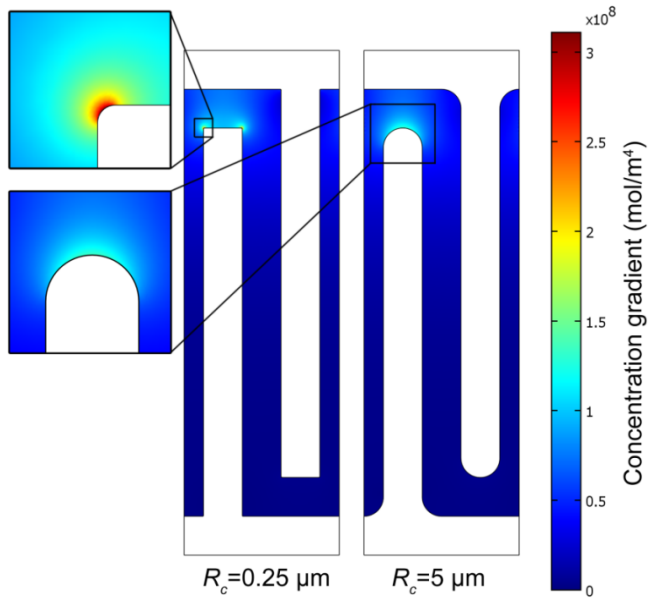
Figure 12. Concentration gradient at steady state in the 3D-trench geometry for sharp and rounded electrode corners. R_c is the radius of curvature of a corner. Insert boxes show magnifications.

3.4. Geometry optimization
by electrode rearrangements

One goal of the 3D-MB design is maximum possible area gain [6]. The trench model is not the best choice for providing it, since the long rectangular plates only have two sides in contact with the electrolyte. To obtain higher electrode surface area, the 3D-interdigitated geometry (Fig. 2a) where the 3D-electrode structure is formed by attaching cylinders or pillars to the electrode base, would be an improvement. The 3D-interdigitated geometry can be constructed in several configurations [7]. For example, the positive and negative electrode pillars could be arranged in rows and facing each other (Figure 4d; a cubic arrangement), the electrode rows could be shifted (Figure 4c) or one pillar could be surrounded by several electrode pillars of opposite charge [7].
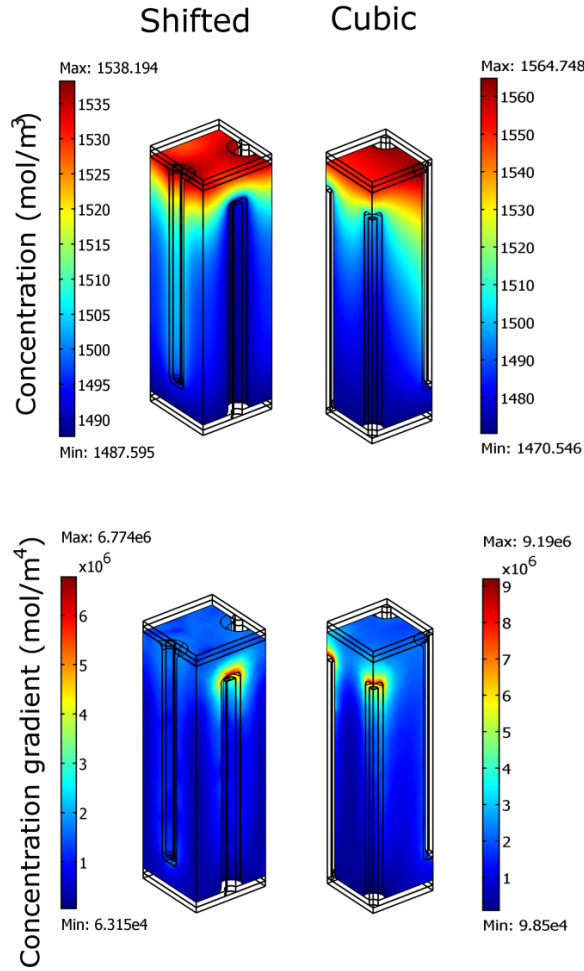
Figure 13. Concentration and concentration gradient in the sifted and cubic 3D-inter-digitated geometry. The shifted geometry demonstrates more uniform electrode surface area utilization.

In Figure 13, the concentration and concentration gradient in the 3D-inter-digitated geometry for two different electrode pillar arrangements are presented [98]. The shifted model gives rise to a more uniform concentration distribution than in the cubic model since all sides of the electrode pillars are equally utilized. The concentration distribution in Figure 13b demonstrates that the shifted model acts somewhat like a "trench" geometry (see for example Figure 6), and every row of pillars acts like a plate with a concentration profile building up between the rows. In the shifted model, the concentration rather builds up around the pillars (see Figure 13). The underutilization of the pillar

sides in the cubic model leads to longer ionic transport pathways, which finally, near the end of the discharge cycle, would increase the resistance of the cell.

The pillar surface area utilization is illustrated in Figure 14, where the numerical values of Eq. 43 are presented. In the shifted geometry, where the current density components in all directions are equal, the R value is close to zero, while the lowest R value in the cubic geometry is ~0.6. The latter result indicates a serious unbalance in the electrode surface utilization – approximately 25% of the surface is underutilized, since the maximum value R is 2.45 (see paragraph 2.3.2).
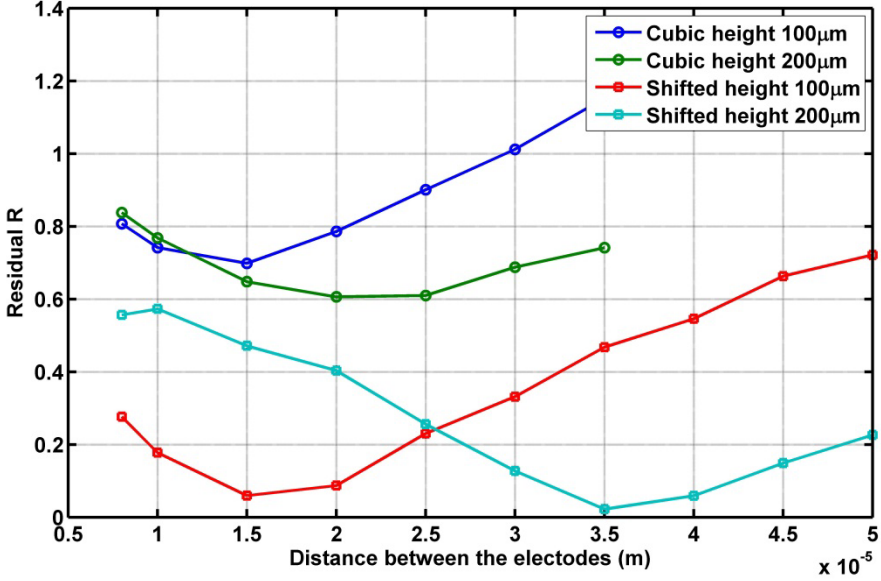

Figure 14. Quantitative performance estimation for cubic and shifted interdigitated geometries. The smallest R-value represents the best geometry.

The ability to make a quantitative evaluation of different geometries is a significant step towards an optimization procedure for the 3D-MB architectures, since every single geometrical change does not have to be evaluated qualitatively. A numerical evaluation makes an automatic selection of suitable geometries possible. For example, the minimum of R in Figure 14 can be estimated by an optimization routine. While the minimization of Eq. 43 proved to be impossible due to its sensitivity to random noise in the gradient based methods used during the multivariable optimization, gradient free single variable optimization methods [99] could be used instead for a fast geometry evaluation. However, these methods tend to converge very slowly during multivariable optimization, motivating implementation of faster optimization algorithms such as structural topology optimization [82].

3.5. The choice of electrolyte

The effect on the concentration distribution by replacing the liquid electrolyte with an ionically conductive polymer in the 3D-MB is presented in Figure 15 (Paper **IV**). In these simulations, a shifted 3D-interdigitated geometry with current collectors inside of the electrodes is used to obtain as homogeneous current density distribution as possible.
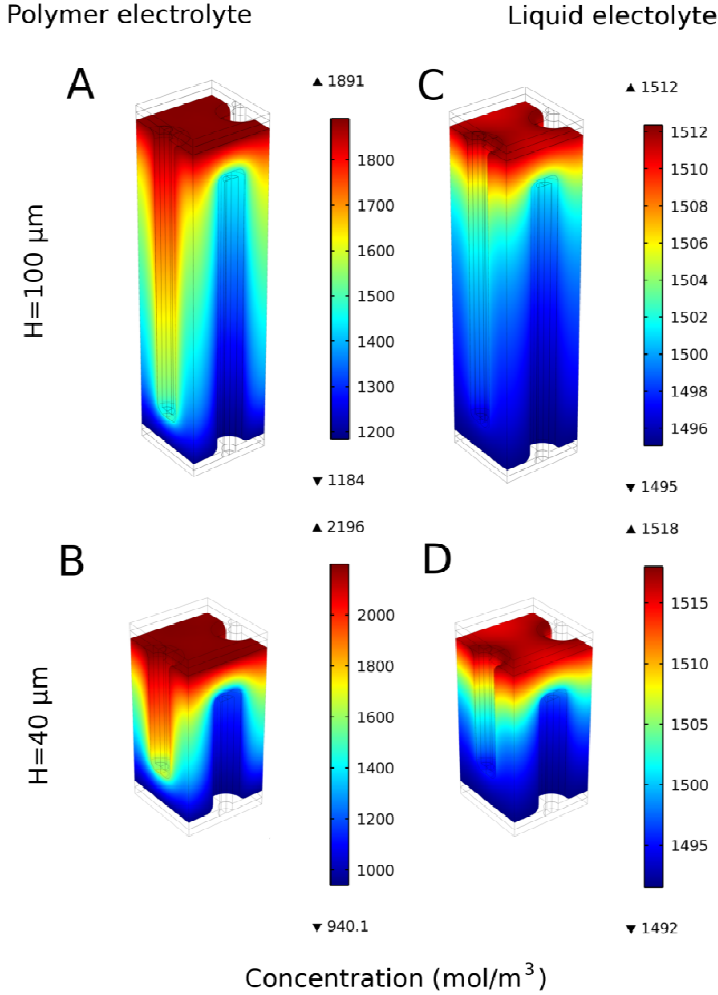

Figure 15. Concentration distribution in 3D-interdigitated geometry with polymer (a and b) and liquid (c and d) electrolytes for pillar height 100 μm (a and c) and 40 μm (b and d). The battery current in the simulations was 10 A/m^2.

49

Figure 15 A and B represents the 3D-MB with polymer electrolyte while C and D represent the cell with liquid electrolyte. The battery current density in these simulations was 10 A/m^2 for both liquid and polymer electrolytes. The lower ionic diffusivity in the polymer electrolyte immediately causes a buildup of a steeper concentration profile than in the liquid electrolyte system – the concentration profile is strongly affected by the 3D electrode structure. In contrast, in the 3D-MB with liquid electrolyte, the concentration distribution is affected mostly by the electrode bases and pillar tips. This effect is more pronounced in the systems with short pillars (Figure 15 D).

It is genuinely characteristic for the concentration distribution in the liquid electrolyte that its most significant changes take place near the base of the positive electrode, while the concentration distribution is almost unchanged over almost the entire pillar lengths. A second feature, originating from the higher conductivity of the liquid electrolyte, is that the concentration distribution is almost independent on the current strength – its maximum deviation from the initial value is only 12 mol/m^3. The concentration distribution in the polymer electrolyte, on the other hand, demonstrates much larger dependence on the discharge current strength. This effect is caused by the much lower diffusion coefficients of the ions in the polymer electrolyte than in the liquid electrolyte. A low polymer electrolyte diffusion coefficient (thereby resulting in a low conductivity) will decrease the maximum battery current, but interestingly, it also displays some positive effects in the 3D-cell. The increased cell resistance facilitates the homogenization of the current density distribution, thereby resulting in a much more homogeneous electrochemical activity. So, the conductive and diffusive properties of the materials are trade-offs in the 3D-MB. On one hand, a high diffusion coefficient makes it possible to achieve stronger currents, but on the other hand, a small diffusion coefficient homo-genizes the electrochemical activity. The ionic conductivity of the polymer electrolyte is low, but when the dimensions of the electrode are downscaled and the charge transport distances become smaller, the low conduction is of less importance.
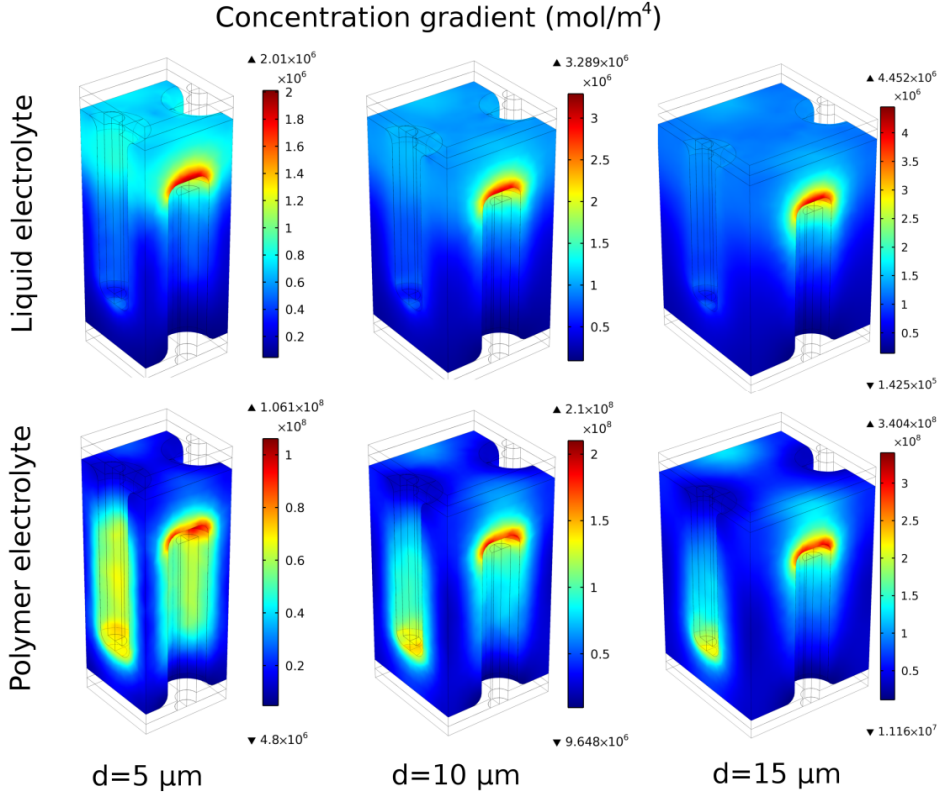
Figure 16. The concentration gradient dependence on the distance between the pillars (*d* is 5 µm, 10 µm and 15 µm) in liquid and polymer electrolytes. The pillar height is 40 µm.

In Figure 16, the concentration gradient distributions in polymer and liquid electrolytes of the 3D-interdigitated geometries with pillar heights of 40 µm are presented. The electrochemical activity in the liquid electrolyte is nonuniformly distributed and is maximal around the tip of the negative electrode, reflecting the concentration and current density distribution discussed above. The electrochemical activity distribution does not depend significantly on the distance between the pillars and is generally similar in all investigated cases. However, its magnitude changes at the negative electrode, since the surface area of the electrode is increased, which results in a decreased local current density.

If using a polymer electrolyte, the concentration gradient distribution depends strongly on the distance between pillars. When *d*=5µm, almost the entire electrode surface is active, while at *d*=15µm only the electrode tips remain active. Such a high sensitivity to the distance between the pillars is caused by the low conductivity of the polymer electrolyte. Since only *d*, not *h*

(Figure 4) is changed, the current chooses the least resistive path when travelling from one electrode to other. Therefore, for d=5μm the shortest distance is to move directly between the pillars, while for d=15μm it is between the pillar tips and electrode bases.

The most uniform concentration gradient distribution is obtained for d=5μm, when most of the pillar surface is active. The lowest concentration gradient values are found at the base of the pillar. Similarly to the trench geometry, this effect is caused by certain features of the geometry. The surface area of the base is much larger than the surface area of the pillar tip, which leads to a small local current density at the bases and a high local current density at the tips. This kind of concentration gradient distribution suggests that the amount of active material in the electrode bases should be decreased and that the amount of active material in the tips should be increased to balance the local material utilization rates, leading to uniform electrochemical activity.

The results from the previous sections lead to the conclusions that the 3D-MB with optimal geometry must fulfill the following requirements:
1. Electrodes with high conductivity, obtained by for example coating current collectors with electrode material.
2. Polymer electrolytes should be used.
3. A shifted interdigitated geometry is better than a cubic arrangement in order to maximize the electrochemical activity over the surface of the pillars.

3.6. Structural topology optimization of the 3D-MB

The evolution of the battery geometry during the structural topology optimization process (described in section 2.3) is presented in Figure 17. The starting point of the optimization is a 3D-trench geometry with uniform material layer coating on the current collectors. In order to achieve as homogeneous current density as possible, the optimization routine starts to rearrange the electrode material. For example, the high current density at the pillar tips at the beginning of the simulation causes the optimization routine to increase the local surface area in order to decrease the local current density. As the optimization continues, more and more material is gathered onto the plates and removed from the bases. Since the current density around the base is low, these parts are underutilized and the electrode material is relocated to the plates. At the end of the optimization routine, almost all electrode material has been removed from the bases and transferred to the plates – only a small island of material remains at the positive electrode base.
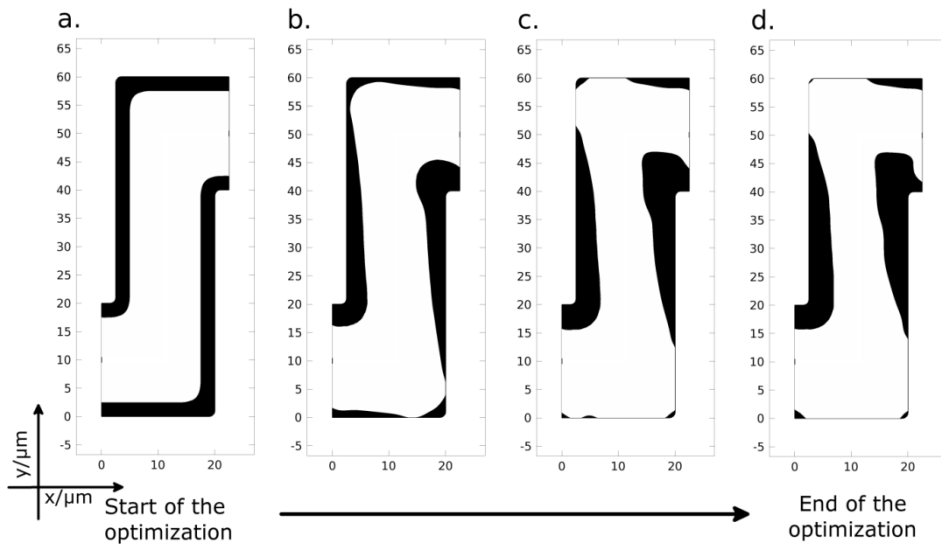
Figure 17. Evolution of the electrode shape during the optimization. Black represents the porous electrode materials and white the electrolyte.

The effect of the optimization can be seen when the ionic transport in the optimized cell and reference cell are compared. *The reference cell* is the starting point of the optimization – a 3D-trench geometry with uniform electrode material layer thickness. The current density distribution, presented in Figure 18 for the optimized (a–c) and reference cells (d–f), displays some distinctive difference for these cases. In the reference cell, the current density distribution changes during the simulation when different parts of the electrodes are being utilized with different rate. At the beginning of discharge, the current density distribution is rather uniform with the highest values at the electrode tips (Figure 18d). As the discharge continues, the tips of the electrode plates are being depleted and the current density distribution is more and more affected by processes at the electrode bases – the current density streamlines in Figure 18e indicate an increased y-component of the current density vector as compared to Figure 18d. This trend continues through the discharge process and is maximum in Figure 18f, where the current is moving mainly between the electrode bases as the tips are fully lithiated. This behavior leads to a significantly increased cell resistance (Paper **V**) since the distance between the bases is considerably longer than the distance between the pillars.
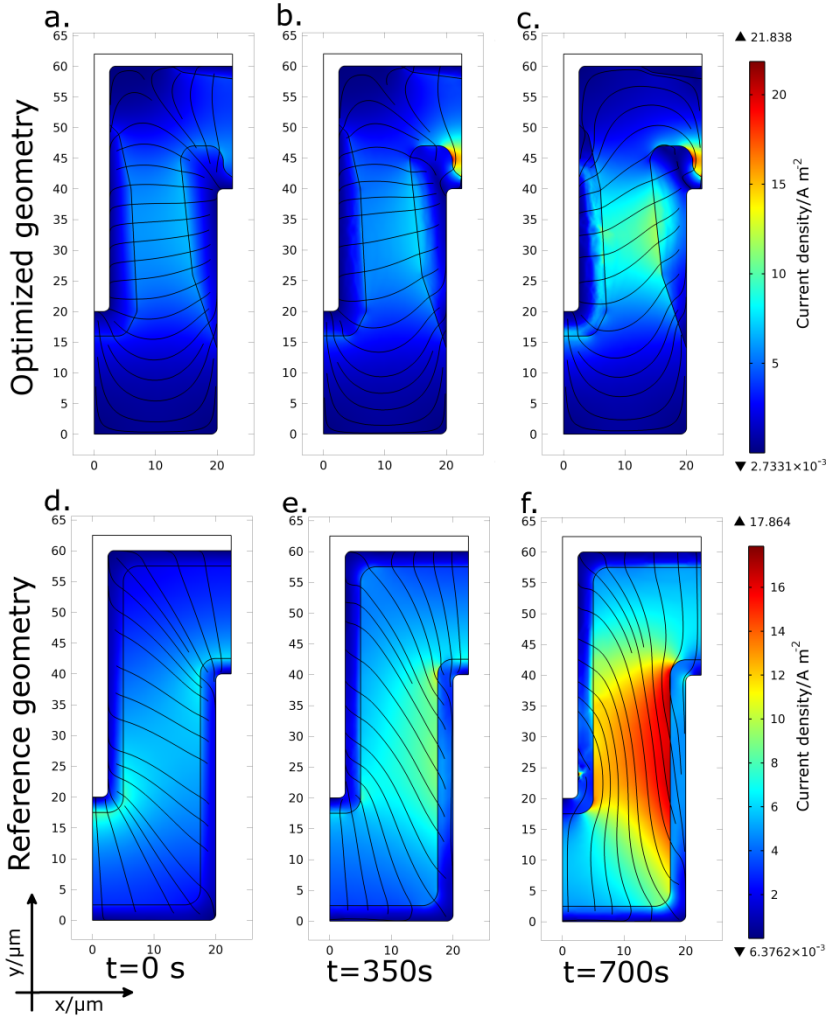
Figure 18. Current density distribution in the electrolyte in optimized (a–c) and reference (d–f) 3D-trench geometries. The streamlines have uniform spacing and represent the current density.

The current density distribution in the reference cell thus demonstrates a complex dynamical evolution, which eventually leads to a decreased performance and poorly utilized electrode materials. The situation is radically different in the optimized geometry. As expected, the current density distribution in the optimized cell is almost uniform and remains stationary during the discharge process. Some minor changes in the current density distribution contribute to a uniform electrode material utilization. This current density distribution is possible only by the application of the topology optimization, which rearranged the electrode material and organized a suitable conductivity distribution.
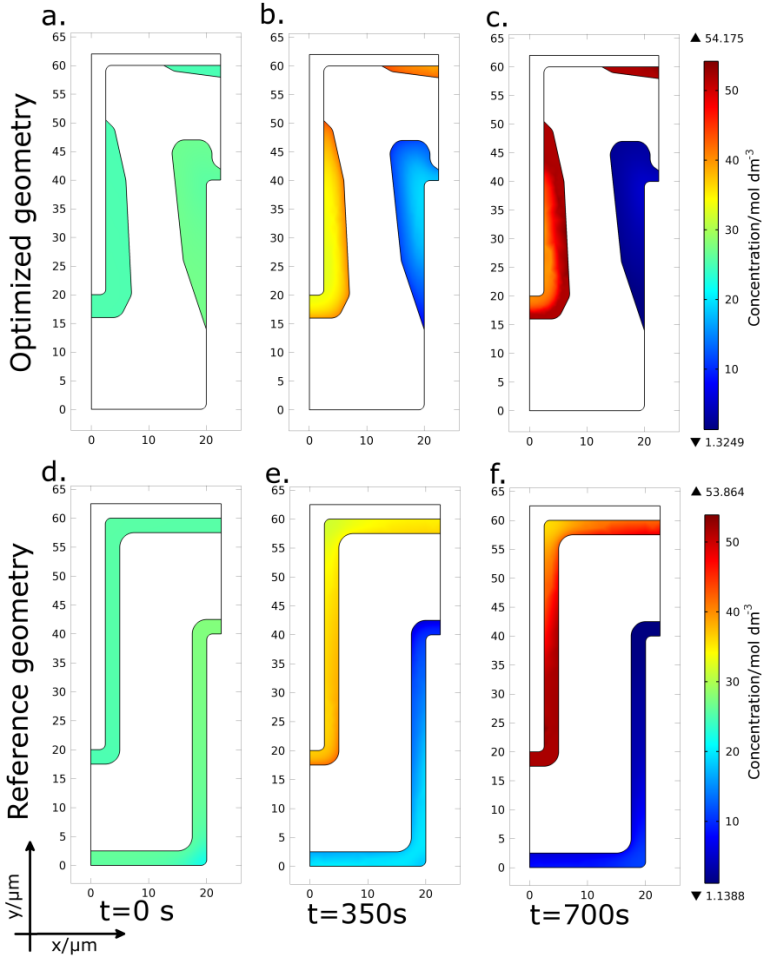
Figure 19. Concentration distribution in the electrodes of optimized (a–c) and reference (d–f) 3D-MB geometries during discharge.

The concentration distribution in the reference (e–f) and optimized cells (a–c) during discharge is presented in Figure 19. At the beginning of the simulation, the concentration distribution is uniform in both geometries. When the discharge continues, the concentration distribution in the reference cell evolves so that the tips of the electrodes are being utilized first (Figure 19e), leading to full lithiation/delithiation of these electrode parts while the electrode bases remains underutilized (Figure 19f). This forces the current to move between electrode bases and increases the overall cell resistance (Paper **V**). In the optimized geometry, on the other hand, *uniform material utilization* is achieved. During the simulation, the electrode material is lithiated/delithiated uniformly over the entire electrode-electrolyte interface (Figure 19b–c). However, due to

that the electrodes are porous, the material utilization is lower at the center of the electrodes (Paper **V**).
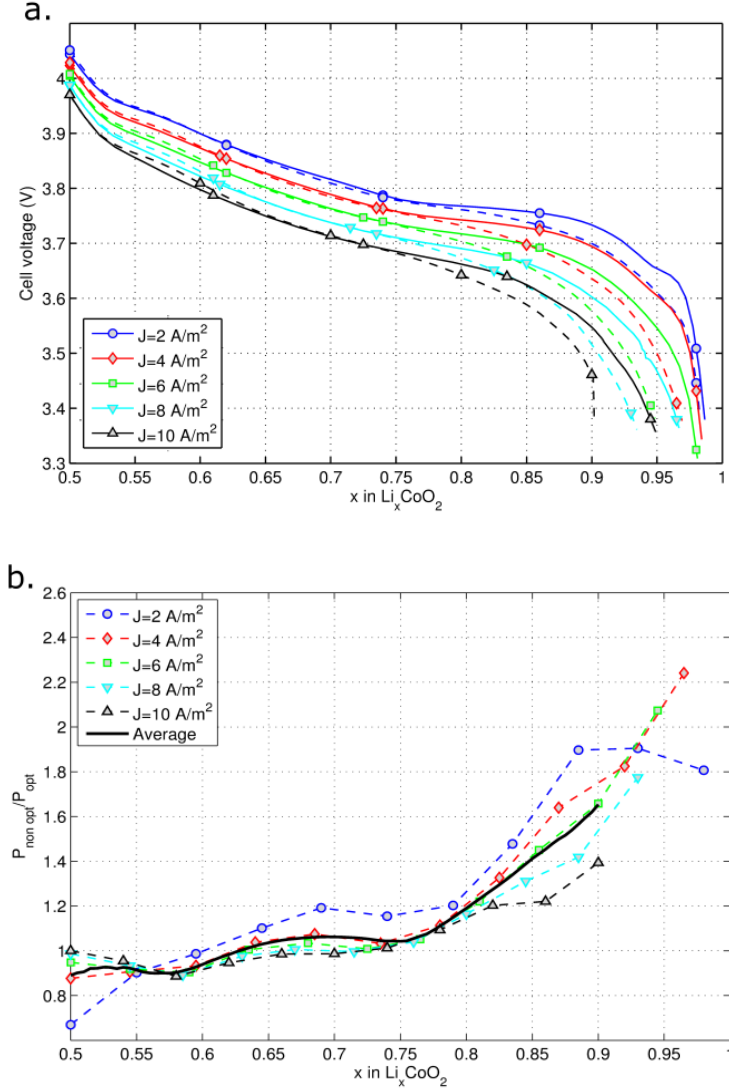

Figure 20. Discharge curves in optimized and reference geometries (left) and performance increase estimation (right). Dashed lines represent the reference geometry and solid lines the optimized geometry.

The impact of the optimization on the cell voltage and the achieved performance gain (Eq. 66) are presented in Figure 20. The discharge starts from $Li_{0.5}CoO_2$ and continues until the cell voltage drops below 3.4 V. Figure 20

56

reveals that the positive effect of the optimization appears in the second half of the discharge, when x>0.75 in Li_xCoO_2. This is when the current in the reference cell starts to move between electrode bases (see Figure 18), and can be seen as a voltage gain for the optimized cell during the discharge process. For example, the optimized cell with a current density of 4 A/m^2 is operating at the same voltage as the reference cell with 2 A/m^2 if x>0.85. Thus, twice as high current can be achieved in the optimized cell during this part of the discharge cycle.

To evaluate the effect of the optimization, the performance gain of the cell (defined in Eq. 66) is presented in Figure 20b. As said above, the optimization does not affect the first half of the discharge cycle; the true effect of the optimization is revealed in the second half of the cycle, where an average performance increase of 1.6 times and a maximum performance increase up to 2.25 times can be seen.

Since the optimization of the geometry is only affecting the second half of the discharge cycle, it can be questioned if it is necessary to conduct any optimization procedure. However, the 3D-MBs are considered for systems requiring high current densities, thus rendering these effects very important. When the devices operate with high current pulses, the active material surface is depleted very fast, which in turn leads to a situation where the battery must operate under conditions where its overall SOC is high, although the local SOC at the electrode-electrolyte interface is low. Under such conditions, the optimized geometry displays significant advantages since the energy dissipated during charge transport is considerably smaller than for the reference cell. Besides generating a longer battery life, higher battery currents and higher cell voltage, the optimization will also result in 3D-MBs with increased safety.

However, it remains to be seen if it is possible fabricate these kinds of cells with unevenly distributed electrode material. Recent contributions from several research groups indicate that when producing electrode coatings, it is not only possible, but maybe even likely, to achieve this kind of depositions rather than completely uniform coatings [100]. For example, Notten and his group fabricated an electrode with slightly thicker material coating at the tips of the plates than at the bottoms of the trenches [19]. Lethien *et al*. [101] synthesized an interdigitated 3D-MB half-cell of silicone nanopillars coated with $LiFePO_4$ and LiPON layers, so that the tips of the pillars had a material coating distribution similar to what was achieved in the simulations presented here. Lafont *et al*. used electrostatic spray pyrolysis to prepare $LiNi_{0.5}Mn_{1.5}O_4$ coated trenches [100], also resulting in a seemingly nonuniform electrode coating. Hopefully, the theoretical work explaining the ionic transport in 3D-MBs with of nonuniformly coated electrodes can simplify future experimental work, and accelerate the research and development in this area by helping to overcome the problems associated with the nonoptimal 3D-battery geometries.

4. CONCLUSIONS

In this thesis, computer simulations of the 3D-MB have been carried out by using the Finite Element Method. 3D-trench and 3D-interdigitated geometries have been simulated and the ionic transport properties during battery operation has been thoroughly investigated. It has been demonstrated that the major differences when utilizing a 3D-geometry as compared to a conventional 2D-design originates in the ionic transport. In a conventional battery, the ionic transport is one-dimensional in nature since the ions move straight between the electrodes. This means that the cell can generally be described by 1D geometrical and mathematical models. However, the 3D electrodes need detailed 3D geometrical models, leading to denser finite element meshes, longer computational times and more complex mathematical descriptions. As a rule of thumb, the demand for computer memory increases by $\sim n^2$, where n is the number of nodes (degrees of freedom). The theoretical part of the work provided algebraic equations to calculate the electrical field and the overpotential in the steady state electrolyte, thereby completely eliminating Ohm's law from the calculations and leaving only one PDE (describing the concentration) to be solved, to describe the ionic transport in the electrolyte, thereby significantly speeding up the computations. This becomes especially important during the structural topology optimization of the 3D-MB, where large numbers of steady state calculation iterations are needed.

The very first simulations of the 3D-trench geometry demonstrated the impact of the electrode conductivity on the ionic transport and the current density distribution in the cell. A constant concentration gradient and a uniform current density in the electrolyte, which are common attributes of thin film batteries, showed to be impossible to achieve when using electrodes of standard Li-ion battery materials such as $LiCoO_2$ (with a conductivity of 0.01 S/m) and LiC_6 (1 S/m). These simulations demonstrated a highly nonuniform current density distribution and material utilization in the 3D-trench geometry, seriously affecting its discharge dynamics and reducing the estimated cell performance. The battery with unmodified electrode conductivity reached the discharge cutoff voltage at 67 % SOC. However, when the conductivity of the positive electrode was increased at least to $\sim$0.25 S/m, *i.e.,* being $\sim$25% of the negative electrode conductivity, almost all effects of the nonuniform current density distribution disappeared.

Furthermore, an almost uniform electrochemical activity was achieved if 3D metal current collectors were coated with the electrode materials. The electrode tips remained slightly more active areas, with the tip of the negative electrode being the most active due to the high electrical conductivity of graphite. However, studies of the discharge dynamics demonstrated that even electrodes with equal conductivities caused nonuniform material utilization. The electrode geometry itself influences the discharging process – the electrode tips are utilized faster than the bases due to local surface area differences.

Also in cells with equal electrode conductivities, a nonuniform electrochemical activity remained near the sharp electrode corners, leading to very high local current densities. The simulations clearly demonstrated how the high electrochemical activity instead was smeared out over the entire electrode tip if the corners were rounded.

The second strategy to achieve a more uniform electrochemical activity was manipulation with the electrode plate height, but this led to serious drawbacks – the positive effect was achieved at the cost of decreasing the amount of active material and a decreased area gain. Thus, the positive effects of utilizing the third dimension diminished.

These results demonstrate the basic tools for investigating ionic transport properties in the 3D-MB. They also identify the basic tools of optimization: manipulations with the material parameters and/or the shape of the electrodes.

One of the key features of the 3D-MB is the surface area gain. However, the area gain is much larger in the 3D-interdigitated than in the 3D-trench geometry, since the pillar sides facing the neighbors contribute to the surface area gain as well. Therefore, the interdigitated geometry is more favorable to use and higher battery currents can be reached. However, the complexity of the geometry is increased due to different possible electrode pillar arrangements. To find the configuration with maximum possible performance, *i.e.,* the cell with uniform electrochemical activity over the electrode surface area, a quantitative cost function was developed and utilized. It provides a tool to evaluate the performance of a 3D-MB geometry configuration using one single numerical value, leading to a quantitative comparison of different geometries. A comparison of shifted and cubic 3D-interdigitated geometries demonstrated clear advantages of the shifted architecture. The cost function value for the shifted geometry was almost zero, while it was ~0.6 for the cubic geometry, indicating that approximately 25% of the surface was underutilized. The method also clearly demonstrated the advantages of the shifted interdigitated geometry over the cubic architecture.

The comparisons of liquid and polymer electrolytes demonstrated the effects of the higher conductivity of the liquid electrolyte. While the concentration of the liquid electrolyte was almost unchanged by the level of the discharging current, the polymer electrolyte developed a significant concentration profile, and the low conductivity of the polymer electrolyte will eventually limit the maximum battery current which can be used. However, the polymer electrolyte displayed some significant advantages as compared to the liquid electrolyte. While a higher conductivity makes it possible to use higher currents, the polymer electrolyte enables constructing the battery with a more uniform current density distribution. The lower electrolyte conductivity forces the electrical current to move through the pillar sides, leading to cells with a high electrochemical activity over the entire electrode surface.

To achieve a uniform material utilization in the electrodes, a topology optimization of the 3D-MB was conducted using the level-set method. Indeed,

the topology optimization suggested a geometry which demonstrated uniform electrode material utilization and an almost stationary current density distribution. However, the nonuniform electrode material coating can be considered a tradeoff. The optimized geometry demonstrated a performance increase up to two times. For example, the same battery voltage could be achieved using 4 A/m^2 discharging current in the optimized geometry and 2 A/m^2 discharging current in the reference cell. The most significant effect of the optimization appeared in the second half of the discharge cycle, which means that the geometry optimization is of special importance when high current pulses are used.

It cannot be claimed that the simulations carried out in this thesis give the total description of the ionic transport in the 3D-MB. For example, there are more geometries than the two considered. An obvious next step would be to continue with simulations of other 3D-MB architectures, for example the 3D-concentric or the aperiodic geometry. More details should also be implemented to the mathematical models. For example, the resistivity of the SEI film layer which has not been simulated here. Interesting results may also be achieved by incorporating concentration dependent diffusion coefficients. Furthermore, as the number of reported prototype cells increases, simulations estimating the performance of experimental cells can be conducted and compared to realistic data. Many of these prototypes have demonstrated problems – for example the interdigitated cell by Min *et al.* [27] which worked only for a couple of cycles and thereafter short-circuited, or the aperiodic geometry [44], which demonstrated similar problems. Now, when the basic properties of the ionic transport in the 3D-microsystems are identified, the bottlenecks for the performance of the experimental geometries can be identified and possible solutions can be suggested. When the optimal electrode material distribution in these geometries is identified, possible problematic locations in the cells can subsequently be identified easily. The main focus of the future 3D-MB studies should therefore be connecting theoretical and experimental work.

5. SUMMARY IN ESTONIAN

3D-mikroaku modelleerimine

Käesolevas väitekirjas on simuleeritud kolmemõõtmelist liitium-ioon akut kasutades Lõplike Elementide Meetodit (LEM). Simulatsioonid on läbi viidud erinevatel geomeetriatel millede tulemusel on põhjalikult uuritud ja karakteriseeritud ioontransporti kolmemõõtmelistes mikrosüsteemides. Üleminekul tavapäraselt akutehnoloogialt kolmemõõtmelisele tehnoloogiale toimub aku elektrolüüdis aset leidvas ioonide transpordis oluline muudatus. Tavaakus toimub ioonide liikumine aku elektroodide vahel mööda sirgjoonelisi trajektoore, mis muudab selle aku oma olemuselt ühemõõtmeliseks ning võimaldab laengu ja massi balanssi akus kirjeldada a ühemõõtmeliste võrrandite abil. 3D-elektroodididega akus muutub olukord see eest, keerulisemaks – ainuüksi selliste elektroodide kasutamine nõuab detailseid 3D-geomeetrilisi mudeleid, mis omakorda nõuab automaatselt kolmemõõtmeliste simulatsioonide läbiviimist ja kolmemõõtmeliste võrrandite kasutamist. Kolmemõõtmelised arvutused on aga aja ning ressursikulukad. Töö teoreetilises osas on välja töötatud algebralised võrrandid leidmaks statsionaarses seisundis elektrolüüdis elektrivälja ja ülepinget. mis võimaldavad statsionaarsetest arvutustest voolutiheduse arvutamise elektrolüüdis täielikult välja jätta. Seega, ioontranspordi täielikuks kirjeldamiseks statsionaarses seisundis elektrolüüdis piisab ainult ühe teist järku osatuletistega diferentsiaalvõrrandi – difusioonivõrrandi – lahendamisest. Selline lähenemine võimaldab olulisel määral kiirendada ning lihtsustada arvutusi ning osutub eriti tähtsaks 3D-aku geomeetria optimeerimise arvutuste käigus mis nõuad suure hulga iteratsioonide läbiviimist.

Üheks olulisemaks parameetriks 3D-akus on elektroodide juhtivus. Juba esimesed simulatsioonid demonstreerisid selle parameetrisuurt mõju voolutiheduse jaotusele terves akus. Tavaakule nii omast ühtlast voolutihedust ei olnud 3D-akus tavapäraseid elektroodimaterjale, nagu $LiCoO_2$ (juhtivusega 0.01 S/m) ja LiC_6 (juhtivus 1 S/m) kasutades võimalik saavutada. Ilmnes, et voolutihedus ning elektroodide laadimine/tühjakslaadimine sellises akus on äärmiselt ebaühtlane ning mõjutab olulisel määral aku tühjakslaadimisdünaamikat ning võimekust. Modifitseerimata elektroodidega aku jõudis tühjenemistsükli lõpuni kui ainult 67% selle teoreetilisest mahtuvusest oli ära kasutatud. Samas, positiivse elektroodi ($LiCoO_2$) juhtivuse tõstmisel vähemalt ~0.25 S/m, õnnestus ebaühtlane voolutiheduse pea-aegu ühtlaseks muuta.

Märkimisväärselt ühtlane elektrokeemiline aktiivsus õnnestus saavutata ka juhul, kui aku geomeetria ülesehitamiseks kasutati kolmemõõtmelisi metallist voolukollektoreid, mis olid kaetud elektroodimaterjaliga. Elektroodide tipud jäid siiski kõige aktiivsemateks piirkondadeks, maksimaalse aktiivsusega negatiivse elektroodi tipus, kuna selle juhtivus oli tunduvalt suurem positiivse elektroodi juhtivusest. Järgnevad tühjakslaadimissimulatsioonid näitasid, et ka võrdsete juhtivustega elektroodide kasutamine ei võimaldanud saavutada

elektroodides ühtlast aktiivse materjali kasutamist. Elektroodide geomeetria ise mõjutas tühjakslaadimisprotsessi – elektroodi sammaste/plaatide tipud tühjenesid kiiremini lokaalsete pindalade erinevuste tõttu elektroodide vahel.

Lisaks materjali juhtivuslike omaduste mõjutamisele osutus üheks elektrokeemilise aktiivsuse homogeniseerimise võimaluseks elektroodi plaatide või sammaste kõrgusega manipuleerimine. Selle meetodi tõsiseks puuduseks osutus asjaolu, et märkimisväärne efekt saavutati alles sammaste/plaatide kõrguse olulisel vähendamisel, mis omakorda vähendas aku mahtuvust ning kahandas kolmanda mõõtme rakendamisega saavutatavat efekti.

Ainuüksi elektroodide juhtivuse võrdsustamisega ei olnud võimalik saavutada täielikult homogeenset elektrokeemilist aktiivsust. Isegi akudes, kus elektroodide juhtivused olid võrdsed, jäid elektroodide teravate nurkade ümbruses olevad alad ebaühtlase elektrokeemilise aktiivsusega piirkondadeks ning põhjustasid kõrgeid lokaalseid voolutihedusi. Simulatsioonidega õnnestus selgelt näidata, et muutes need teravad nurgad ümarateks, jaotatakse elektrokeemiline aktiivsus üle terve elektroodi tipu ning lokaalsed voolutihedused ühtlustatakse.

Need tulemused illustreerivad ilmekalt põhilisi joontranspordi omadusi 3D akudes ning näitavad, milliseid meetodeid rakendades on võimalik 3D-mikroaku geomeetria optimiseerida. Sobivad tehnikad on manipuleerimine elektroodimaterjali juhtivusega ning elektroodide geomeetriliste parameetrite või kujuga.

Üheks olulisemaks 3D-mikroaku karakteristikuks on kolmemõõtmelise elektroodi geomeetria kasutamisega saavutatav *pindalavõit*, mis on erinevate akugeomeetriate puhul erinev. Näiteks, kolmemõõtmelise sammastega geomeetria puhul on see palju suurem, kui kolmemõõtmeliste plaatidega geomeetria korral. Nimelt, viimases on elektroodile kolmas mõõde antud plaadikujuliste liidestega mistõttu elektrolüüdiga saavad kontakti moodustada ainult plaadi servad. Kolmemõõtmeliste sammastega geomeetria puhul on aga saavutatakse elektroodi kolmas mõõde sellele sammaste/silindrite lisamise. Sellise lahenduse puhul on aga elektrolüüdiga kontaktis olev pindala märkimisväärselt suurem. Samas, selle geomeetria kasutamisel suureneb koheselt ka geomeetria keerukus kuna koheselt tekivad erinevad võimalused sammaste paigutamiseks. Leidmaks konfiguratsiooni, mis tagab maksimaalse võimekuse leiti kvantitatiivne sihifunktsioon mida rakendati erinevate kolmemõõtmeliste geomeetriate uurimiseks. Võrdlus erinevate sammastega geomeetriate vahel näitas, et nn. nihutatud geomeetria omab märkimisväärset eelist võrreldes kuubikulise arhitektuuriga. Sihifunktsiooni väärtus nihutatud geomeetria puhul oli praktiliselt null, samas kui kuubikulise geomeetria puhul oli selleks ~0.6, mis näitab et umbkaudu 25% pinnas oli alakasutatud. Seega, praktilistes lahendustes tuleks eelistada nihutatud geomeetriat kuubikulisele.

Vedelate ja polümeer elektrolüütide võrdlus demonstreeris ilmekalt vedela elektrolüüdi parema juhtivuse mõju. Samal ajal, kui akut läbiv vool ioonide kontsentratsiooni vedelas elektrolüüdis pea-aegu ei mõjutanud, arenes polümeerelektrolüüdis oluline kontsentratsiooniprofiil. Seega, polümeerelektrolüüdi

halb juhtivus hakkaks piirama akut läbivat voolu varem kui samaväärne vool hakkaks vedelale elektrolüüdile mingitki olulist mõju vedelale avaldama. Hoolimata juhtivuslikest probleemidest oli polümeer elektrolüüdil vedela ees ka olulisi eeliseid. Kui vedel elektrolüüt võimaldas kasutada kõrgemaid voolusid, siis polümeer elektrolüüt tagas ühtlasema voolutiheduse jaotuse saavutamise. Polümeer elektrolüüdi madal juhtivus sundis elektrivoolu liikuma läbi elektroodi sammaste külgede, mitte läbi tippude, nagu vedela elektrolüüdi puhul. Selle tulemusena saavutati ühtlasem eletrokeemiline aktiivsus üle terve elektroodi pinna, mis omakorda võimaldas saavutada ühtlasemat elektroodimaterjali kasutust.

Täielikult ühtlase elektroodimaterjali kasutuse saavutamiseks, viidi läbi 3D-mikroaku elektroodide geomeetria optimiseerimine. Optimeerimise tulemusena osutus võimalikuks koostada selline aku elektroodide konstruktsioon, mille puhul saavutati elektrolüüdis pea-aegu täielikult statsionaarne voolutiheduse jaotus ning ühtlane elektroodide laadumine/tühjakslaadumine. Samas, efekt saavutati ebaühtlase paksusega elektroodide kasutamise tõttu. Geomeetria optimeerimise rakendamine võimaldas saavutada kuni kahekordse aku võimekuse kasvu. Näiteks, võrdne aku pinge saavutati juhtudel, kui optimeeritud ja optimeerimata geomeetriaga akusid laeti tühjaks kasutades vastaval 4 A/m^2 ja 2 A/m^2 suurust tühjakslaadimisvoolu. Optimeerimise kõige olulisem mõju avaldus tühjakslaadimistsükli teises pooles, mis tähendab, et optimeeritud geomeetria kasutamine omandab erilise tähtsuse aku suurte voolutugevustega laadimisel/tühjakslaadimisel või kõrgete vooluimpulsside puhul.

Oleks ennatlik väita, käesoleva väitekirja raames läbi viidud simulatsioonid annavad 3D-mirkoakus ammendava ülevaate. Näiteks, antud töös käsitleti ainult kahte geomeetriat. Järgmiseks loomulikuks sammuks oleks seega teiste arhitektuuride simuleerimine, näiteks 3D-kontsentrilise geomeetria ja aperioodilise geomeetria modelleerimine. Matemaatilist mudelit tuleks muuta detailsemaks – näiteks elektroodide ja elektrolüüdi vahelise pinnakihi taksitus tuleks arvutustesse lisada. Huvitavaid tulemusi võib saada ka juhul, kui kasutada kontsentratsioonist sõltuvaid difusioonikoefitsiente. Lisaks, viimasel ajal on hakanud suurenema eksperimentaalsete 3D-mikroaku prototüüpide hulk. Paljudel nendest prototüüpidest on olnud tõsiseid probleeme – Min *et al*. [27] ehitasid 3D-mikroaku, mis töötas ainult paar tühjakslaadimistsüklit ning seejärel lühistus. Aperioodiline geomeetria [44] näitas üles sarnaseid probleeme. Nüüd kui põhilised ioontranspordi omadused 3D-mikrosüsteemides on identifitseeritud on võimalike probleemide leidmine lihtsam. Tulevikus läbi viidavate simulatsioonide kõige olulisemaks eesmärgiks peaks olema teoreetiliste ja eksperimentaalsete tööde ühendamine.

6. ACKNOWLEDGMENTS

7. APPENDIX I

Table 1. Parameters used in simulations

Symbol	Quantity	Value
D_{Li}	Diffusion constant for Li$^+$ ions in the polymer electrolyte [97]	$2.5 \cdot 10^{-13}$ m^2/s
	Diffusion constant for Li$^+$ ions in the liquid electrolyte [63]	$2.5 \cdot 10^{-11}$ m^2/s
D_{PF6}	Diffusion constant for PF$_6^-$ ions in the polymer electrolyte [97]	$3 \cdot 10^{-13}$ m^2/s
	Diffusion constant for PF$_6^-$ ions in the liqid electrolyte [63]	$3 \cdot 10^{-11}$ m^2/s
D	Li diffusion constant in the active material [96]	$2.5 \cdot 10^{-13}$ m^2/s
σ_{Al}	Electronic conductivity of the positive current collector (Al) [57]	$3.75 \cdot 10^7$ S/m
σ_p	Electronic conductivity of the positive electrode active material (LiCoO$_2$) [96]	$1 \cdot 10^{-2}$ S/m
σ_n	Electronic conductivity of the negative electrode (LiC$_6$) [96]	1 S/m
σ_{Cu}	Electronic conductivity of the negative current collector (Cu) [57]	$5.95 \cdot 10^7$ S/m
c_0	Salt concentration in the electrolyte	1.5 M
j_0	Discharge current during optimization	10 A/m^2
ε	Porosity of the electrodes	0.5
i_0	Exchange current density during optimization	100 A/m^2
k	Rate coefficient during discharge simulations	$2 \cdot 10^{-11}$ m/s
$c_{s,\max}^p$	Maximum Li concentration in the active material of the positive electrode	51656 mol/m^3
$c_{s,\max}^n$	Maximum Li concentration in the active material of the negative electrode	28225 mol/m^3
ε_{ls}	Parameter controlling electrode-electrolyte interface thickness during optimization (for validation)	$0.5 \cdot 10^{-6}$ m ($1 \cdot 10^{-6}$m)
γ	Reinitialization parameter during optimization (for validation).	100 m/s (40 m/s)
H	The geometrical parameters, explained in Figure 4	$20 \cdot 10^{-6}$m – $100 \cdot 10^{-6}$m
d,h		$5 \cdot 10^{-6}$m–$15 \cdot 10^{-6}$m
d_c		$1 \cdot 10^{-6}$m (if applicable)
$(d–h)/2$		$2.5 \cdot 10^{-6}$m

8. REFERENCES

[1]   A. Volta, On the Electricity Excited by the Mere Contact of Conducting Substances of Different Kinds. In a Letter from Mr. Alexander Volta, F. R. S. Professor of Natural Philosophy in the University of Pavia, to the Rt. Hon. Sir Joseph Banks, Bart. K. B. P. R. S., *Phil. Trans. R. Soc. Lond.* 90 (1800) 403–431.

[2]   G. Planté, Note sur la polarisation voltaique, in: Comptes Rendus Hebdomadaires Des Séances De l'Académie Des Sciences, Paris, 1859: pp. 402–405.

[3]   G. Planté, Nouvelle pile secondaire d'une grande puissance, in: Comptes Rendus Hebdomadaires Des Séances De l'Académie Des Sciences, Paris, 1860: pp. 640–642.

[4]   K. Mizushima, P.C. Jones, P.J. Wiseman, J.B. Goodenough, Li_xCoO_2 (0<–1): A new cathode material for batteries of high energy density, *Mater. Res. Bull.* 15 (1980) 783–789.

[5]   Intel® Core^{TM} i7-920 Processor (8M Cache, 2.66 GHz, 4.80 GT/s Intel® QPI), *http://ark.intel.com/products/37147/Intel-Core-i7-920-Processor-(8M-Cache-2_66-GHz-4_80-GTs-Intel-QPI)*.

[6]   J.W. Long, B. Dunn, D.R. Rolison, H.S. White, Three-Dimensional Battery Architectures, *Chem. Rev.* 104 (2004) 4463–4492.

[7]   R.W. Hart, H.S. White, B. Dunn, D.R. Rolison, 3-D Microbatteries, *Electrochem. Commun.* 5 (2003) 120–123.

[8]   M. Roberts, P. Johns, J. Owen, D. Brandell, K. Edstrom, G.E. Enany, C. Guery, D. Golodnitsky, M. Lacey, C. Lecoeur, H. Mazor, E. Peled, E. Perre, M.M. Shaijumon, P. Simon, P.-L. Taberna, 3D lithium ion batteries—from fundamentals to fabrication, *J. Mater. Chem.* 21 (2011).

[9]   E.A. Johannessen, Lei Wang, Li Cui, Tong Boon Tang, M. Ahmadian, A. Astaras, S.W.. Reid, P.S. Yam, A.F. Murray, B.W. Flynn, S.P. Beaumont, D.R.. Cumming, J.M. Cooper, Implementation of multichannel sensors for remote biomedical measurements in a microsystems format, *IEEE Trans. Biomed. Eng.* 51 (2004) 525–535.

[10] D.F. Lemmerhirt, K.D. Wise, Chip-Scale Integration of Data-Gathering Microsystems, *Proc. IEEE*. 94 (2006) 1138–1159.

[11] P. Mohseni, K. Najafi, S.J. Eliades, Xiaoqin Wang, Wireless multichannel biopotential recording using an integrated FM telemetry circuit, *IEEE Trans. Neural Syst. Rehabil. Eng.* 13 (2005) 263–271.

[12] H. Sato, C.W. Berry, B.E. Casey, G. Lavella, Ying Yao, J.M. VandenBrooks, M.M. Maharbiz, A cyborg beetle: Insect flight control through an implantable, tetherless microsystem, in: IEEE 21st International Conference on Micro Electro Mechanical Systems, 2008. MEMS 2008, IEEE, 2008: pp. 164–167.

[13] T.S. Arthur, D.J. Bates, N. Cirigliano, D.C. Johnson, P. Malati, J.M. Mosby, E. Perre, M.T. Rawls, A.L. Prieto, B. Dunn, Three-Dimensional Electrodes and Battery Architectures, *MRS Bulletin*. 36 (2011) 523–531.

[14] H. Mazor, D. Golodnitsky, L. Burstein, E. Peled, High Power Copper Sulfide Cathodes for Thin-Film Microbatteries, *Electrochem. Solid-State Lett.* 12 (2009) A232–A235.

[15] M. Nathan, D. Golodnitsky, V. Yufit, E. Strauss, T. Ripenbein, I. Shechtman, S. Menkin, E. Peled, Three-dimensional thin-film Li-ion microbatteries for autonomous MEMS, *J. Microelectromech. Syst.* 14 (2005) 879–885.

[16]   D. Golodnitsky, M. Nathan, V. Yufit, E. Strauss, K. Freedman, L. Burstein, A. Gladkich, E. Peled, Progress in three-dimensional (3D) Li-ion microbatteries, *Solid State Ionics*. 177 (2006) 2811–2819.

[17]   D. Golodnitsky, V. Yufit, M. Nathan, I. Shechtman, T. Ripenbein, E. Strauss, S. Menkin, E. Peled, Advanced materials for the 3D microbattery, *J. Power Sources* 153 (2006) 281–287.

[18]   P.H.L. Notten, F. Roozeboom, R.A.H. Niessen, L. Baggetto, 3-D Integrated All-Solid-State Rechargeable Batteries, *Adv. Mater.* 19 (2007) 4564–4567.

[19]   J.F.M. Oudenhoven, L. Baggetto, P.H.L. Notten, All-Solid-State Lithium-Ion Microbatteries: A Review of Various Three-Dimensional Concepts, *Adv. Energy Mater.* 1 (2011) 10–33.

[20]   L. Baggetto, R.A.H. Niessen, F. Roozeboom, P.H.L. Notten, High Energy Density All-Solid-State Batteries: A Challenging Concept Towards 3D Integration, *Adv. Funct. Mater.* 18 (2008) 1057–1066.

[21]   L. Baggetto, J.F.M. Oudenhoven, T. van Dongen, J.H. Klootwijk, M. Mulder, R.A.H. Niessen, M.H.J.M. de Croon, P.H.L. Notten, On the electrochemistry of an anode stack for all-solid-state 3D-integrated batteries, *J. Power Sources*. 189 (2009) 402–410.

[22]   P. Johns, M. Roberts, J. Owen, Conformal electrodeposition of manganese dioxide onto reticulated vitreous carbon for 3D microbattery applications, *J. Mater. Chem.* 21 (2011) 10153–10159.

[23]   J.W. Long, D.R. Rolison, Architectural Design, Interior Decoration, and Three-Dimensional Plumbing en Route to Multifunctional Nanoarchitectures, *Acc. Chem. Res.* 40 (2007) 854–862.

[24]   F. Chamran, Yuting Yeh, Hong-Seok Min, B. Dunn, Chang-Jin Kim, Fabrication of High-Aspect-Ratio Electrode Arrays for Three-Dimensional Microbatteries, *J. Microelectromech. Syst.* 16 (2007) 844–852.

[25]   P.L. Taberna, S. Mitra, P. Poizot, P. Simon, J.-M. Tarascon, High rate capabilities Fe_3O_4-based Cu nano-architectured electrodes for lithium-ion battery applications, *Nat Mater*. 5 (2006) 567–573.

[26]   G.T. Teixidor, R.B. Zaouk, B.Y. Park, M.J. Madou, Fabrication and characterization of three-dimensional carbon electrodes for lithium-ion batteries, *J. Power Sources* 183 (2008) 730–740.

[27]   H.-S. Min, B.Y. Park, L. Taherabadi, C. Wang, Y. Yeh, R. Zaouk, M.J. Madou, B. Dunn, Fabrication and properties of a carbon/polypyrrole three-dimensional microbattery, *J. Power Sources* 178 (2008) 795–800.

[28]   T. Ohzuku, R.J. Brodd, An overview of positive-electrode materials for advanced lithium-ion batteries, *J. Power Sources* 174 (2007) 449–456.

[29]   E. Antolini, $LiCoO_2$: formation, structure, lithium and oxygen nonstoichiometry, electrochemical behaviour and transport properties, *Solid State Ionics*. 170 (2004) 159–171.

[30]   G. Amatucci, J.-M. Tarascon, Optimization of Insertion Compounds Such as $LiMn_2O_4$ for Li-Ion Batteries, *J. Electrochem. Soc.* 149 (2002) K31–K46.

[31]   A.K. Padhi, Phospho-olivines as Positive-Electrode Materials for Rechargeable Lithium Batteries, *J. Electrochem. Soc.* 144 (1997) 1188.

[32]   P.G. Dickens, S.J. French, A.T. Hight, M.F. Pye, Phase relationships in the ambient temperature $Li_xV_2O_5$ system (0.1<1.0), *Mater. Res. Bull.* 14 (1979) 1295–1299.

[33] S.K. Cheah, E. Perre, M. Rooth, M. Fondell, A. Hårsta, L. Nyholm, M. Boman, T. Gustafsson, J. Lu, P. Simon, K. Edström, Self-Supported Three-Dimensional Nanoelectrodes for Microbattery Applications, *Nano Lett.* 9 (2009) 3230–3233.

[34] E. Perre, P.L. Taberna, D. Mazouzi, P. Poizot, T. Gustafsson, K. Edström, P. Simon, Electrodeposited Cu_2Sb as Anode Material for 3-Dimensional Li-Ion Microbatteries, *J. Mater. Res.* 25 (2010) 1485–1491.

[35] S. Tan, S. Walus, J. Hilborn, T. Gustafsson, D. Brandell, Poly(ether amine) and cross-linked poly(propylene oxide) diacrylate thin-film polymer electrolyte for 3D-microbatteries, *Electrochem. Commun.* 12 (2010) 1498–1500.

[36] E. Perre, L. Nyholm, T. Gustafsson, P.-L. Taberna, P. Simon, K. Edström, Direct electrodeposition of aluminium nano-rods, *Electrochem. Commun.* 10 (2008) 1467–1470.

[37] M.-S. Wu, P.-C.J. Chiang, J.-T. Lee, J.-C. Lin, Synthesis of Manganese Oxide Electrodes with Interconnected Nanowire Structure as an Anode Material for Rechargeable Lithium Ion Batteries, *J. Phys. Chem. B*. 109 (2005) 23279–23284.

[38] M.M. Shaijumon, E. Perre, B. Daffos, P. Taberna, J. Tarascon, P. Simon, Nanoarchitectured 3D Cathodes for Li-Ion Microbatteries, *Adv. Mater.* 22 (2010) 4978–4981.

[39] L.-F. Cui, Y. Yang, C.-M. Hsu, Y. Cui, Carbon−Silicon Core−Shell Nanowires as High Capacity Electrode for Lithium Ion Batteries, *Nano Lett.* 9 (2009) 3370–3374.

[40] M. Nishizawa, K. Mukai, S. Kuwabata, C.R. Martin, H. Yoneyama, Template Synthesis of Polypyrrole-Coated Spinel $LiMn_2O_4$ Nanotubules and Their Properties as Cathode Active Materials for Lithium Batteries, *J. Electrochem. Soc.* 144 (1997) 1923–1927.

[41] N. Li, C.R. Martin, B. Scrosati, A High-Rate, High-Capacity, Nanostructured Tin Oxide Electrode, *Electrochem. Solid-State Lett.* 3 (2000) 316–318.

[42] M. Kotobuki, Y. Suzuki, H. Munakata, K. Kanamura, Y. Sato, K. Yamamoto, T. Yoshida, Effect of sol composition on solid electrode/solid electrolyte interface for all-solid-state lithium ion battery, *Electrochim. Acta* 56 (2011) 1023–1029.

[43] F. Chamran, Hong-Seok Min, B. Dunn, Chang-Jin Kim, Zinc-air microbattery with electrode array of zinc microposts, in: IEEE 20th International Conference on Micro Electro Mechanical Systems, 2007. MEMS, IEEE, 2007: pp. 871–874.

[44] P. Johns, M.J. Lacey, M.R. Roberts, G. Enany, J.R. Owen, Self-assembly of lithium batteries with 3D architecture, *18th International Conference on Solid State Ionics* (2011) 302.

[45] G. Turon Teixidor, B.Y. Park, P.P. Mukherjee, Q. Kang, M.J. Madou, Modeling fractal electrodes for Li-ion batteries, *Electrochim. Acta* 54 (2009) 5928–5936.

[46] V. Springel, S.D.M. White, A. Jenkins, C.S. Frenk, N. Yoshida, L. Gao, J. Navarro, R. Thacker, D. Croton, J. Helly, J.A. Peacock, S. Cole, P. Thomas, H. Couchman, A. Evrard, J. Colberg, F. Pearce, Simulations of the formation, evolution and clustering of galaxies and quasars, *Nature* 435 (2005) 629–636.

[47] R.M. Martin, Electronic Structure: Basic Theory and Practical Methods, Cambridge University Press, Cambridge, 2005.

[48] D.C. Rapaport, The Art of Molecular Dynamics Simulation, 2nd ed., Cambridge University Press, 2004.

[49] CSE – The DL_POLY Molecular Simulation Package, *http://www.stfc.ac.uk/CSE/randd/ccg/software/DL_POLY/25526.aspx*.

[50] CSE – The DL_MESO Mesoscale Simulation Package, *http://www.stfc.ac.uk/CSE/randd/ccg/software/DL_MESO/25522.aspx*.

[51] C. Grossmann, H.-G. Roos, M. Stynes, Numerical Treatment of Partial Differential Equations, 1st ed., Springer, 2007.

[52] S.S. Quek, G.R. Liu, Finite Element Method: A Practical Course, 1st ed., Butterworth-Heinemann, 2003.

[53] S.S. Rao, The Finite Element Method in Engineering, Fourth Edition, 4th ed., Butterworth-Heinemann, 2004.

[54] P.-B. Zhou, Numerical Analysis of Electromagnetic Fields, Springer-Verlag, 1993.

[55] A. Tveito, R. Winther, Introduction to Partial Differential Equations: A Computational Approach, 1st ed., Springer, 1998.

[56] H.J. Bergveld, W.S. Kruijt, P.H.L. Notten, Electronic-network modelling of rechargeable NiCd cells and its application to the design of battery management systems, *J. Power Sources* 77 (1999) 143–158.

[57] Multiphysics Modeling and Simulation Software – COMSOL, *Http://www.comsol.com/*.

[58] K.E. Jansen, C.H. Whiting, G.M. Hulbert, A generalized-[alpha] method for integrating the filtered Navier-Stokes equations with a stabilized finite element method, *Comput. Meth. Appl. Mech. Eng.* 190 (2000) 305–319.

[59] J. Chung, G.M. Hulbert, A Time Integration Algorithm for Structural Dynamics With Improved Numerical Dissipation: The Generalized-alpha Method, *J. Appl. Mech.* 60 (1993) 371–375.

[60] A.C. Hindmarsh, P.N. Brown, K.E. Grant, S.L. Lee, R. Serban, D.E. Shumaker, C.S. Woodward, SUNDIALS: Suite of nonlinear and differential/algebraic equation solvers, *ACM Trans. Math. Softw.* 31 (2005) 363–396.

[61] P.N. Brown, A.C. Hindmarsh, L.R. Petzold, Using Krylov Methods in the Solution of Large-Scale Differential-Algebraic Systems, *SIAM J. Sci. Comput.* 15 (1994) 1467–1488.

[62] A.J. Bard, L.R. Faulkner, Electrochemical Methods: Fundamentals and Applications, 2nd ed., Wiley, 2000.

[63] D. Danilov, P.H.L. Notten, Mathematical modelling of ionic transport in the electrolyte of Li-ion batteries, *Electrochim. Acta* 53 (2008) 5569–5578.

[64] M. Doyle, T.F. Fuller, J. Newman, Modeling of galvanostatic charge and discharge of the lithium/polymer/insertion cell, *J. Electrochem. Soc.* 140 (1993) 1526–33.

[65] T.F. Fuller, M. Doyle, J. Newman, Simulation and optimization of the dual lithium ion insertion cell, *J. Electrochem. Soc.* 141 (1994) 1–10.

[66] M. Doyle, J. Newman, A.S. Gozdz, C.N. Schmutz, J.-M. Tarascon, Comparison of modeling predictions with experimental data from plastic lithium ion cells, *J. Electrochem. Soc.* 143 (1996) 1890–903.

[67] P. Arora, M. Doyle, A.S. Gozdz, R.E. White, J. Newman, Comparison between computer simulations and experimental data for high-rate discharges of plastic lithium-ion batteries, *J. Power Sources* 88 (2000) 219–231.

[68] P.M. Gomadam, J.W. Weidner, R.A. Dougal, R.E. White, Mathematical modeling of lithium-ion and nickel battery systems, *J. Power Sources* 110 (2002) 267–284.

[69] W. Lai, F. Ciucci, Mathematical modeling of porous battery electrodes – Revisit of Newman's model, *Electrochim. Acta* 56 (2011) 4369–4377.

[70] W. van Schalkwijk, B. Scrosati, Advances in Lithium-Ion Batteries, 1st ed., Springer, 2002.

[71] Q. Zhang, Q. Guo, R.E. White, Semi-empirical modeling of charge and discharge profiles for a $LiCoO_2$ electrode, *J. Power Sources* 165 (2007) 427–435.

[72] C.-W. Wang, A.M. Sastrya, Mesoscale modeling of a Li-ion polymer cell, *J. Electrochem. Soc.* 154 (2007) 1035–47.

[73] K.A. Smith, C.D. Rahn, C.-Y. Wang, Control oriented 1D electrochemical model of lithium ion battery, *Energy Convers. Manage.* 48 (2007) 2565–2578.

[74] N. Munichandraiah, L.G. Scanlon, R.A. Marsh, B. Kumar, A.K. Sircar, Determination of the exchange current density of the $Li^+ + e^- \leftrightarrow Li$ reaction in polymer electrolytes by galvanostatic linear polarization of symmetrical cells, *J. Electroanal. Chem.* 379 (1994) 495–499.

[75] P. Georén, G. Lindbergh, Characterisation and modelling of the transport properties in lithium battery polymer electrolytes, *Electrochim. Acta* 47 (2001) 577–587.

[76] A. Nyman, M. Behm, G. Lindbergh, Electrochemical characterisation and modelling of the mass transport phenomena in $LiPF_6$-EC-EMC electrolyte, *Electrochim. Acta* 53 (2008) 6356–6365.

[77] A.T. Stamps, S. Santhanagopalan, E.P. Gatzke, Using Piecewise Polynomials to Model Open-Circuit Potential Data, *J. Electrochem. Soc.* 154 (2007) P20–P27.

[78] T.F. Coleman, Y. Li, On the convergence of interior-reflective Newton methods for nonlinear minimization subject to bounds, *Math. Program.* 67 (1994) 189–224.

[79] T.F. Coleman, Y. Li, An Interior Trust Region Approach for Nonlinear Minimization Subject to Bounds, *SIAM J. Optimiz.* 6 (1996) 418–445.

[80] D.E. Goldberg, Genetic Algorithms in Search, Optimization, and Machine Learning, Addison-Wesley, 1989.

[81] S. Kirkpatrick, C.D. Gelatt, M.P. Vecchi, Optimization by Simulated Annealing, *Science*. 220 (1983) 671–680.

[82] M.P. Bendsøe, O. Sigmund, Topology optimization: theory, methods, and applications, Springer, 2003.

[83] M.P. Bendsøe, Optimal shape design as a material distribution problem, *Struct. Multidiscip. O.* 1 (1989) 193–202.

[84] T.E. Bruns, A reevaluation of the SIMP method with filtering and an alternative formulation for solid–void topology optimization, *Struct. Multidiscip. O.* 30 (2005) 428–436.

[85] O. Sigmund, A 99 line topology optimization code written in Matlab, *Struct. Multidiscip. O.* 21 (2001) 120–127.

[86] S.J. Osher, F. Santosa, Level Set Methods for Optimization Problems Involving Geometry and Constraints: I. Frequencies of a Two-Density Inhomogeneous Drum, *J. Comput. Phys.* 171 (2001) 272–288.

[87] M.Y. Wang, X. Wang, D. Guo, A level set method for structural topology optimization, *Comput. Meth. Appl. Mech. Eng.* 192 (2003) 227–246.

[88] Z. Liu, J.G. Korvink, R. Huang, Structure topology optimization: fully coupled level set method via FEMLAB, *Struct. Multidiscip. O.* 29 (2005) 407–417.

[89] E. Olsson, G. Kreiss, A conservative level set method for two phase flow, *J. Comput. Phys.* 210 (2005) 225–246.

[90] E. Olsson, G. Kreiss, S. Zahedi, A conservative level set method for two phase flow II, *J. Comput. Phys.* 225 (2007) 785–807.

[91]   C. Zhuang, Z. Xiong, H. Ding, A level set method for topology optimization of heat conduction problem under multiple load cases, *Comput. Meth. Appl. Mech. Eng.* 196 (2007) 1074–1084.

[92]   Z. Luo, L. Tong, H. Ma, Shape and topology optimization for electrothermomechanical microactuators using level set methods, *J. Comput. Phys.* 228 (2009) 3173–3181.

[93]   F. Okkels, H. Bruus, Scaling behavior of optimally structured catalytic microfluidic reactors, *Phys. Rev. E.* (2006).

[94]   L.H. Olesen, F. Okkels, H. Bruus, A high-level programming-language implementation of topology optimization applied to steady-state Navier-Stokes flow, *Int. J. Numer. Methods Eng.* 65 (2006) 975–1001.

[95]   T.E. Bruns, Topology optimization of convection-dominated, steady-state heat transfer problems, *Int. J. Heat Mass Tran.* 50 (2007) 2859–2873.

[96]   M. Park, X. Zhang, M. Chung, G.B. Less, A.M. Sastry, A review of conduction phenomena in Li-ion batteries, *J. Power Sources* 195 (2010) 7904–7929.

[97]   J. Karo, D. Brandell, A Molecular Dynamics study of the influence of side-chain length and spacing on lithium mobility in non-crystalline $LiPF_6 \cdot PEO_x$; x = 10 and 30, *Solid State Ionics.* 180 (2009) 1272–1284.

[98]   V. Zadin, H. Kasemägi, A. Aabloo, D. Brandell, Modeling the 3D-Microbattery by Finite Element Methodology, *ECS Meeting Abstracts* 1003 (2010) 684.

[99]   J.C. Lagarias, J.A. Reeds, M.H. Wright, P.E. Wright, Convergence Properties of the Nelder–Mead Simplex Method in Low Dimensions, *SIAM J. Optimiz.* 9 (1998) 112–147.

[100] U. Lafont, A. Anastasopol, E. Garcia-Tamayo, E. Kelder, Electrostatic spray pyrolysis of $LiNi_{0.5}Mn_{1.5}O_4$ films for 3D Li-ion microbatteries, *Thin Solid Films.* 520 (2012) 3464–3471.

[101] C. Lethien, M. Zegaoui, P. Roussel, P. Tilmant, N. Rolland, P.A. Rolland, Micropatterning of LiPON and lithium iron phosphate material deposited onto silicon nanopillars array for lithium ion solid state 3D micro-battery, *Microelectron. Eng.* 88 (2011) 3172–3177.

PUBLICATIONS

CURRICULUM VITAE

Name	Vahur Zadin
Date of birth	06/12/1982
Phone	+372 55 544 178
E-mail	zadin@ut.ee

Career

Institution and position held
2008– … PhD student at Tartu University. In periods, guest doctoral student at the Technical University of Eindhoven, Netherlands, and Uppsala University, Sweden
2006–2008 Estonian University of Life Sciences; specialist (0.75)
2005–2006 State Agency of Medicines; specialist (1.00)

Education
2008–... University of Tartu, doctoral studies
2005–2008 University of Tartu, masters studies, physics
2000–2005 University of Tartu, bachelor studies, physics

Scientific activity
Vahur Zadin, Master's Degree, 2008, (sup) **Jüri Vedru**, Foucalult' kardiogrammi tekke uuringud südant sondeerivate pöörisvoolude arvutamise abil (A study of Foucault' cardiogram origination by calculating eddy currents in the heart region), **University of Tartu**

Languages
Estonian – native language
English – speaking good, writing good, understanding excellent
German – speaking poor, writing poor, understanding poor
Russian – speaking poor, writing poor, understanding poor

Research
Natural Sciences and Engineering, Chemistry and Chemical Technology(Optimization of Lithium-Ion battery architecture by computer simulations.
http://www.ims.ut.ee/mediawiki/index.php/User:Vahur)

CURRICULUM VITAE

Nimi	Vahur Zadin
Sünniaeg	06/12/1982
Telefon	+372 55 544 178
E-mail	zadin@ut.ee

Teensituskäik 2008– … doktorant Tartu Ülikoolis. Perioodiliselt külalisdoktorant Eindhoveni Tehnikaülikoolis (Holland) ja Uppsala Ülikoolis (Rootsi)
2006–2008 Eesti Maaülikool; spetsialist (0.75)
2005–2006 Ravimiamet; spetsialist (1.00)

Haridus 2008–... Tartu Ülikool, doktorantuur
2005–2008 Tartu Ülikool, magistrantuur, füüsika
2000–2005 Tartu Ülikool, bakalaureuseõpe, füüsika

Teaduslik ja arendustegevus **Vahur Zadin**, magistrikraad, 2008, (sup) **Jüri Vedru**, Foucalult' kardiogrammi tekke uuringud südant sondeerivate pöörisvoolude arvutamise abil (A study of Foucault' cardiogram origination by calculating eddy currents in the heart region), **University of Tartu**

Keelteoskus Eesti keel – emakeel
Inglise keel – hea
Saksa keel – halb
Vene keel – halb

Peamised uurimis-valdkonnad Peamiseks uurimisvaldkonnaks doktoriõpingute käigus on 3D liitium-ioon akude ahrhitektuuri optimeerimine arvutisimulatsioonide põhjal. Peamiseks matemaatiliseks töövahendiks on seejuures lõplike elementide meetod (http://www.ims.ut.ee/mediawiki/index.php/User:Vahur).

Uurimisvaldkonnaks magistriõpingute käigus oli Foucault' kardiograafia uurimine arvutisimulatsioonide abil, kasutades lõplike elementide meetodit.

DISSERTATIONES TECHNOLOGIAE
UNIVERSITATIS TARTUENSIS

1. **Imre Mäger.** Characterization of cell-penetrating peptides: Assessment of cellular internalization kinetics, mechanisms and bioactivity. Tartu 2011, 132 p.
2. **Taavi Lehto.** Delivery of nucleic acids by cell-penetrating peptides: application in modulation of gene expression. Tartu 2011, 155 p.
3. **Hannes Luidalepp**. Studies on the antibiotic susceptibility of *Escherichia coli*. Tartu 2012, 111 p.